*J. metamorphic Geol.*, 2006, **24,** 633–654 doi:10.1111/j.1525-1314.2006.00659.x

# Multistage metamorphism of the Huangtuling granulite, Northern Dabie Orogen, eastern China: implications for the tectonometamorphic evolution of subducted lower continental crust

Y. CHEN,[1] K. YE,[1] J.-B. LIU[1] AND M. SUN[2]
[1]*State Key Laboratory of Lithospheric Evolution, Institute of Geology and Geophysics, Chinese Academy of Sciences, PO Box 9825, Beijing 100029, China (yekai@mail.iggcas.ac.cn)*
[2]*Department of Earth Sciences, University of Hong Kong, Hong Kong, China*

**ABSTRACT** Granulites from Huangtuling in the North Dabie metamorphic core complex in eastern China preserve rare mineralogical and mineral chemical evidence for multistage metamorphism related to Palaeoproterozoic metamorphic processes, Triassic continental subduction-collision and Cretaceous collapse of the Dabie Orogen. Six stages of metamorphism are resolved, based on detailed mineralogical and petrological studies: (I) amphibolite facies (6.3–7.0 kbar, 520–550 °C); (II) high-pressure/high-temperature granulite facies (12–15.5 kbar, 920–980 °C); (III) cooling and decompression (4.8–6.0 kbar, 630–700 °C); (IV) medium-pressure granulite facies (7.7–9.0 kbar, 690–790 °C); (V) low-pressure/high-temperature granulite facies (4.0–4.7 kbar, 860–920 °C); (VI) retrograde greenschist facies overprint (1–2 kbar, 340–370 °C). The *P–T* history derived in this study and existing geochronological data indicate that the Huangtuling granulite records two cycles of orogenic crustal thickening events. The earlier three stages of metamorphism define a clockwise *P–T* path, implying crustal thickening and thinning events, possibly related to the assembly and breakup of the Columbia Supercontinent at *c.* 2000 Ma. Stage IV metamorphism indicates another crustal thickening event, which is attributed to Triassic subduction/collision between the Yangtze and Sino-Korean Cratons. The dry lower crustal granulite persisted metastably during the Triassic subduction/collision because of the lack of hydrous fluid and deformation. Stage V metamorphism records the Cretaceous collapse of the Dabie Orogen, possibly due to asthenosphere upwelling or removal of the lithospheric mantle resulting in heating of the granulite and partial melting of the North Dabie metamorphic core complex. Comparison of the Huangtuling granulite in North Dabie and the high-pressure–ultrahigh-pressure metamorphic rocks in South Dabie indicates that the subducted upper (South Dabie) and lower (North Dabie) continental crusts underwent contrasting tectonometamorphic evolution during continental subduction-collision and orogenic collapse.

**Key words:** Dabie Orogen; granulite; multistage metamorphism; subducted lower continental crust.

## INTRODUCTION

The subduction of continental crust commonly results in the formation of high-pressure (HP)–ultrahigh-pressure (UHP) metamorphic rocks (see review of Carswell & Compagnoni, 2003). However, based on petrological and geochemical investigations, the protoliths of HP–UHP rocks are mainly of supracrustal origin (Liou, 1999; Ernst, 2001; Zhang *et al.*, 2002; Rolfo *et al.*, 2004). In young and active collisional orogens such as the Himalayas (O'Brien, 2001; Myrow *et al.*, 2003) and Alps (Pfiffner *et al.*, 2000; O'Brien, 2001), UHP rocks of subducted upper continental crust are exhumed back to the Earth's surface or shallow crustal levels, whereas the rocks of subducted lower continental crust remain buried deeply in orogens, forming the basement of the over-thickened crustal mountain root (Zhao & Nelson, 1993; Nelson *et al.*, 1996; Pfiffner *et al.*, 2000). This root remains stable long after its formation in some old collisional orogens, such as the Late Devonian to Permian south Ural Mountains (Berzin *et al.*, 1996; Echtler *et al.*, 1996; Knapp *et al.*, 1998) and the Precambrian southern Trans-Hudson orogen (Nelson *et al.*, 1993; Baird *et al.*, 1996). In contrast, the continental crust has returned to a normal thickness, in other mature subduction-collision orogens such as the Dabie Orogen in eastern China (Gao *et al.*, 1998; Ratschbacher *et al.*, 2000; Wang *et al.*, 2000), and the Caledonian (Milnes

Mineral abbreviations used in this paper are after Kretz (1983).

 

*et al.*, 1997; Andersen, 1998; White & Hodges, 2003) and Variscan (Nelson, 1992; Brown & Dallmeyer, 1996; Le Pichon *et al.*, 1997) orogens in Europe. In mature subduction-collision orogens such as the Dabie Orogen, older HP and UHP terranes (South Dabie in the Dabie Orogen) are comprised mainly of rocks from the subducted upper continental crust, whereas the younger post-orogenic metamorphic core complex with granulite (North Dabie in the Dabie Orogen) is comprised mainly of rocks from the subducted lower continental crust. The metamorphic core complex exhibits extensive post-orogenic extensional structures and concomitant magmatism and/or anatexis. These observations suggest that the subducted upper and lower continental crust underwent contrasting tectonometamorphic evolution in the processes of continental subduction, collision and subsequent collapse of the orogen. A great deal of research, concerning the occurrence of UHP index minerals, metamorphic petrology and tectonic evolution has been devoted to the HP–UHP rocks. However, less attention had been paid to the metamorphic core complex component of these mature orogens. The tectonometamorphic evolution of the subducted lower continental crust and its role in the processes of continental subduction, collision and orogenic collapse is still enigmatic.

Rare granulite occurs as lenses of metres to tens of metres in size within migmatitic gneiss in the North Dabie metamorphic core complex in eastern China (Zhang *et al.*, 1996; Chen *et al.*, 1998). Geochemical and geochronological analyses indicate that the protolith of the granulites is the Precambrian basement rock of the subducted Yangtze Craton (Ma *et al.*, 2000; Zhang *et al.*, 2002). These granulites provide an opportunity to explore the tectonometamorphic evolution of lower continental crust involved in the processes of continental subduction, collision and collapse in the Dabie Orogen.

Chen *et al.* (1998) reported that granulite from Huangtuling in the North Dabie metamorphic core complex underwent two stages of granulite facies metamorphism, an early high-pressure stage and a later low-pressure stage, which are attributed to Triassic subduction and decompressional exhumation of the Yangtze Craton. In this paper, the *P–T* evolution of the Huangtuling granulite is established based on detailed mineralogical and petrological investigations, and the tectonometamorphic history is constrained by a combination of the *P–T* path and available geochronological data. Our new data indicate that the Huangtuling granulite has preserved rare textural and mineralogical evidences of six stages of metamorphism related to two orogenic cycles from Early Precambrian to Late Mesozoic. These new data enable us to investigate the roles of the subducted lower continental crust in the processes of continental subduction, collision and collapse in the Dabie Orogen.

## GEOLOGICAL SETTING

The Dabie–Sulu Orogen in east-central China is regarded as the largest UHP metamorphic terrane in the world (see review of Carswell & Compagnoni, 2003). The orogen was formed by combination of the Triassic northward subduction/collision of the Yangtze Craton beneath the Sino-Korean Craton, and Cretaceous reactivation by extensional unroofing of the North Dabie metamorphic core complex (Hacker *et al.*, 1998, 2000; Ratschbacher *et al.*, 2000). The Dabie Orogen is composed of several petrotectonic units (Fig. 1). From south to north these are: a greenschist to blueschist facies metamorphic terrane; a high-pressure amphibolite facies metamorphic terrane; a quartz–eclogite facies metamorphic terrane; a coesite–eclogite facies metamorphic terrane; the North Dabie metamorphic core complex; and the North Huaiyang belt, composed of low-grade metamorphic flysch deposits or passive continental apron deposits of the Yangtze Craton (Okay *et al.*, 1993; Zheng *et al.*, 2005). Surface geology demonstrates that overall the orogen displays a Cretaceous NW–SE subhorizontal extensional structure, with the southern HP and UHP terranes and the northern North Huaiyang belt overlying the North Dabie Complex (Hacker *et al.*, 1998, 2000; Ratschbacher *et al.*, 2000). All the metamorphic terranes are intruded by Cretaceous granitoids (Zhang *et al.*, 2002).

The greenschist–blueschist to coesite–eclogite terranes in the South Dabie comprise a variety of continent crustal rocks of the Yangtze Craton, which were subducted and metamorphosed under low-*P* to UHP conditions around 240–230 Ma (Li *et al.*, 1993, 2000; Rowley *et al.*, 1997; Xue *et al.*, 1997; Hacker *et al.*, 1998; Ayers *et al.*, 2002). Geochemical and Sr–Nd–Pb isotopic characteristics of the HP and UHP rocks indicate that their protoliths are of upper crustal origin (Baker *et al.*, 1997; Yui *et al.*, 1997; Zheng *et al.*, 1998; Ma *et al.*, 2000; Zhang *et al.*, 2002). The upper crustal origin of the HP and UHP rocks implies that the upper part of the subducted continental crust may have decoupled from the lower crust during the Triassic subduction-collision.

The North Dabie metamorphic core complex consists dominantly of gneisses of tonalite–trondhjemite–granite compositions exhibiting varying degrees of migmatization that are intensively intruded by Cretaceous granitoid and mafic–ultramafic plutons (Hacker *et al.*, 1998, 2000; Jahn *et al.*, 1999; Ratschbacher *et al.*, 2000). The age of migmatization and uplift of the North Dabie metamorphic core complex is 137–112 Ma (Xue *et al.*, 1997; Hacker *et al.*, 1998; Zhao *et al.*, 2005). Relict lenses of garnet–granulite, magnetite–quartzite (banded iron formation) and marble occur sporadically in the migmatite (Zhang *et al.*, 1996). Geochemical and Nd–Sr–Pb isotope data show that the majority of the rocks in the North Dabie metamorphic core complex are distinct from those in

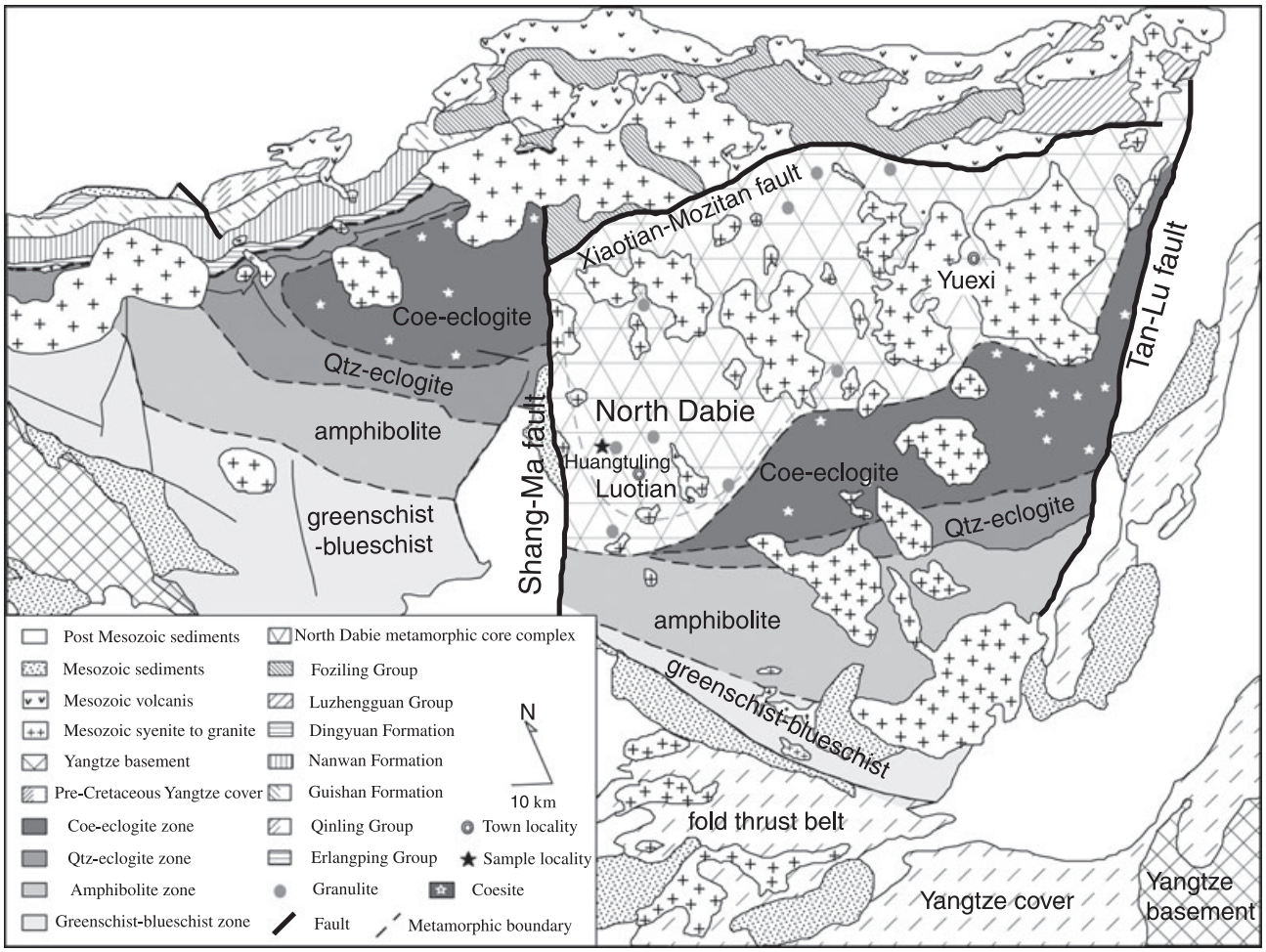


**Fig. 1.** Geological sketch map of the Dabie orogen in eastern China with the granulite localities in the North Dabie metamorphic core complex.

the HP and UHP terranes. Zhang *et al.* (2002) demonstrated that the isotopic compositions of gneisses from the North Dabie metamorphic core complex are of lower continental crust affinity. The granulite relicts have similar Nd model ages and Nd–Sr isotopic compositions to those of the Kongling complex, which is believed to be the Precambrian basement rock of the Yangtze Craton (Ma *et al.*, 2000; Zhang *et al.*, 2002).

The granulites were sampled from Huangtuling in North Dabie metamorphic core complex (Fig. 1). The granulite occurs as a 10 m long lensoid body in granitic migmatitic gneiss. It consists of discontinuously intercalated plagioclase–quartz-rich leucosome and garnet–orthopyroxene–biotite-rich melanosome. Ten centimetre-wide late granitic dykes, formed by the migmatization of the country gneiss, cut the foliation of the granulite. Chen *et al.* (1998) reported that the Huangtuling granulite underwent two stages of granulite facies metamorphism. The earlier high-pressure granulite facies metamorphism is characterized by predominant coarse-grained garnet + orthopyroxene + plagioclase + biotite + K-feldspar + quartz. The *P–T* conditions are estimated to be 13.5 ± 2 kbar and 850 ± 50 °C, which are attributed to Triassic subduction and collision of the Yangtze Craton (Chen *et al.*, 1998). A later weak granulite overprint is documented by the rim replacement of earlier coarse-grained garnet by very fine-grained cordierite, orthopyroxene, plagioclase and biotite, attributed to exhumational decompression of the subducted Yangtze Craton (Chen *et al.*, 1998). However, these interpretations are not supported by dating, as no Triassic ages have been reported from the Huangtuling granulite.

## PETROGRAPHY

On a hand-specimen scale, the granulite has a layered structure, defined by alternative mm to cm scale compositional layers rich in garnet + orthopyroxene + biotite and plagioclase + quartz. The granulite shows weak deformation, only coarse-grained plagioclase and quartz are weakly elongated.

The granulite is mainly composed of garnet (10–15%), orthopyroxene (10–15%), biotite (10–15%), plagioclase (25%), K-feldspar (5%) and quartz (25%) with minor cordierite (5%), rutile (< 1%), ilmenite (< 1%), kyanite (< 1%), spinel (< 1%) and pyrite (1–2%). The granulites preserve multistage disequilibrium textures.

Rare porphyroblastic garnet, which is up to 2 cm in diameter, is preserved in the matrix of medium-grained (up to 3 mm) garnet, orthopyroxene, biotite, plagioclase, K-feldspar and quartz (Fig. 2a). The core of the porphyroblastic garnet contains abundant minute (20–80 $\mu$m) inclusions of amphibole, muscovite, biotite, plagioclase, quartz and ilmenite (Fig. 2b). The inclu-

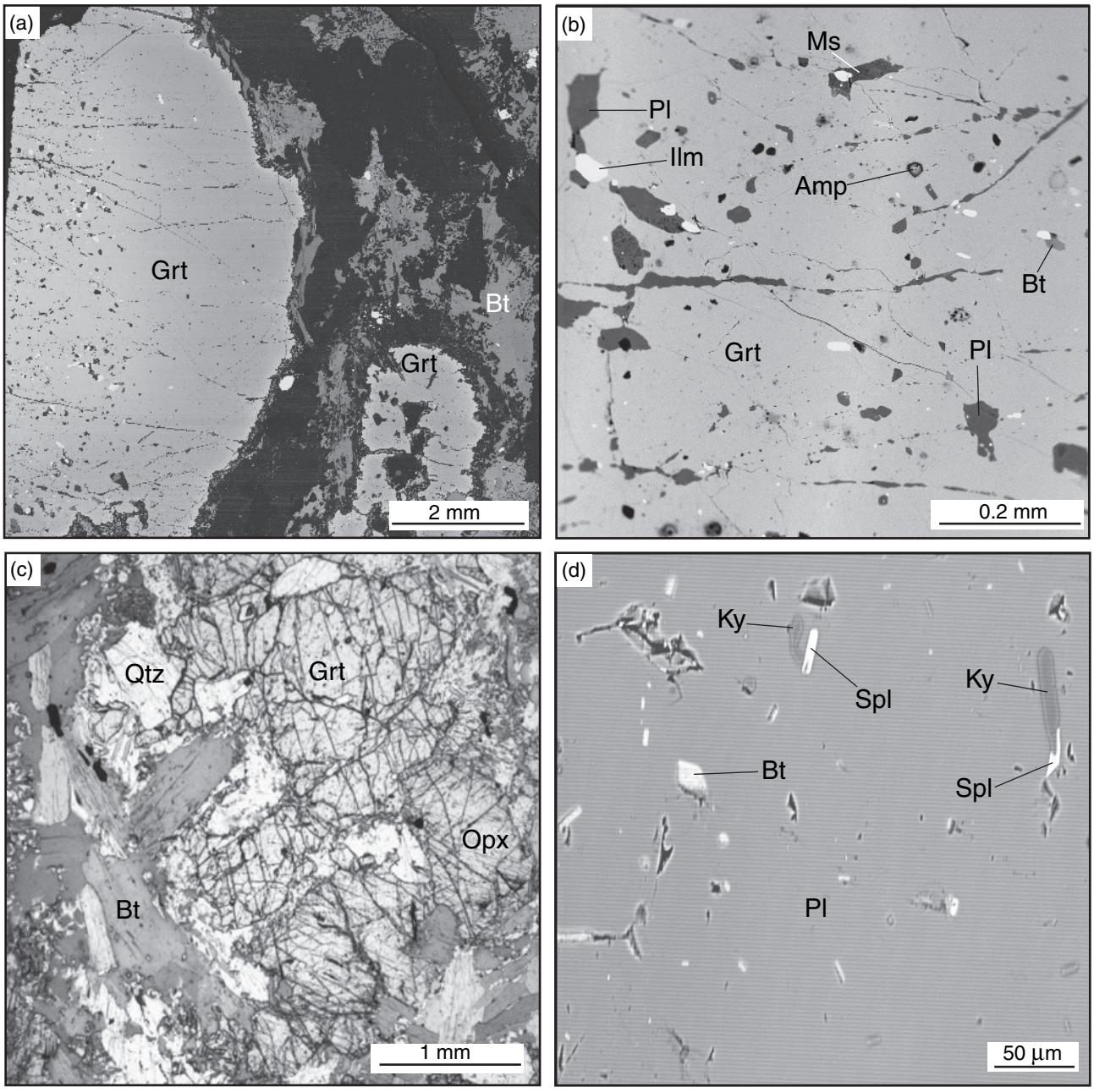


**Fig. 2.** (a) Back-scattered electron image showing textures of the Huangtuling granulite (sample HTL11a). The core of the porphyroblastic garnet contains abundant inclusions, but only rare inclusions in the mantle, and the rim is replaced by fine-grained symplectites. (b) Back-scattered electron image showing inclusions of muscovite, biotite, plagioclase, amphibole, ilmenite and quartz in the core of porphyroblastic garnet (sample HTL11a). (c) Photomicrograph showing matrix garnet, orthopyroxene, biotite and plagioclase (sample HTL13); symplectites occur along rims and fractures in garnet. (d) Kyanite needles associated with acicular spinel in plagioclase cores (sample HTL24).

sions define the first-generation mineral assemblage in the rocks, which predates the mantle of porphyroblastic garnet and the medium-grained matrix minerals. The mantle of the porphyroblastic garnet rarely contains inclusions of orthopyroxene, biotite, plagioclase and rutile, the rim is inclusion free.

Medium-grained garnet, orthopyroxene, biotite, plagioclase, K-feldspar and quartz in the matrix constitute the main minerals of the granulite (Fig. 2c). The core of the matrix garnet commonly contains similar mineral inclusions to the mantle of the porphyroblastic garnet: orthopyroxene, biotite, plagioclase, rutile and quartz. Fine-grained kyanite occurs rarely in the core of the matrix garnet. Coronitic plagioclase commonly develops between quartz inclusions and host garnet, suggesting that plagioclase was produced by reaction of garnet and quartz during decompression (Chen *et al*., 1998; Fu *et al*., 2003). The core of the matrix orthopyroxene includes biotite and garnet, whereas its rim includes fine-grained rounded plagioclase and quartz. Very fine ilmenite exsolution rods are restricted to the core of matrix orthopyroxene. The matrix biotite is interpreted to be in equilibrium with garnet and orthopyroxene; rutile rods are common in biotite cores. The matrix feldspar is dominated by plagioclase with rare K-feldspar. Cores of the matrix K-feldspar occasionally contain albite lamellae, whereas rims are free of lamellae. Fine-grained kyanite and spinel occur as acicular inclusions in the cores of the matrix plagioclase (Fig. 2d).

In samples weakly overprinted by late symplectite (e.g. HTL24), coronitic garnet occurs between medium-grained matrix plagioclase and mafic phases, such as orthopyroxene (Fig. 3a,b), biotite (Fig. 3c,d) and pyrite (Fig. 3e,f). Abundant minute inclusions of quartz and rare plagioclase occur in the coronitic garnet (Fig. 3b,d). Rare biotite also occurs in the coronitic garnet surrounding biotite (Fig. 3d). The plagioclase rim in contact with coronitic garnet contains abundant quartz inclusions, however, quartz is absent in plagioclase away from the coronitic garnet. The coronitic garnet is consumed by later symplectite in samples strongly overprinted by later-stage metamorphism.

Most samples exhibit some overprinting characterized by fine-grained ($< 50$ $\mu$m) symplectite, inferred to record decompression. The symplectite is rare in samples that preserve coronitic garnet (e.g. HTL19 and HTL24). In samples strongly overprinted by symplectite (e.g. HTL11a & HTL13), the rims of porphyroblastic, medium-grained and coronitic garnet exhibit partial replacement by vermicular symplectites of Opx + Crd + Bt, Crd + Bt + Spl + Qtz or Opx + Crd + Bt + Pl (Fig. 4a–f). These symplectites develop in limited areas (100–200 $\mu$m) and usually divide primary garnet into fragments. Fine-grained (5–10 $\mu$m) spinel in direct contact with quartz and cordierite occurs in the symplectites after garnet (Fig. 4c,d). Symplectites of orthopyroxene + cordierite or orthopyroxene + cordierite + quartz replace matrix biotite (Fig. 5a,b); abundant quartz inclusions always occur in the plagioclase adjacent to the symplectite.

A weak greenschist facies retrogression is present in most samples. The retrograde metamorphic effects include: (1) replacement of Crd–Bt–Qtz symplectite by muscovite, chlorite, albite and calcite; (2) the occurrence of fine-grained biotite along the rim or cleavage planes of orthopyroxene; and (3) the replacement of biotite by chlorite. No foliation has been observed associated with the greenschist facies minerals.

## MINERAL CHEMISTRY

Mineral compositions were analysed using a CAMECA SX-51 microprobe analyzer in the Institute of Geology and Geophysics, Chinese Academy of Sciences. Analytical conditions were 15 kV accelerating voltage, 20 nA beam current and 20 s counting time for most minerals; 12 nA beam current was used for plagioclase and K-feldspar to avoid Na migration. Representative compositions of garnet, orthopyroxene, mica, feldspar, cordierite, amphibole and spinel are presented in Tables 1–6, respectively.

### Garnet

Representative compositions of the three textural types of garnet are plotted in Fig. 6. Porphyroblastic garnet is zoned. Figures 7(a) and 8(a) show the zonation for half a typical porphyroblastic garnet. The inner core (approximately 500 $\mu$m) is almandine-rich ($Alm_{63-65}Prp_{21-23}Grs_{11-12}Sps_2$) (Table 1; Fig. 6). Line traverses (200–300 $\mu$m) across the garnet core near biotite and plagioclase inclusions do not show any clear chemical zoning. The inner part of the outer core is homogeneous in grossular. However, grossular decreases from through the outermost core (Fig. 8a). Almandine decreases gradually in the outer core, which is compensated by increasing pyrope. The mantle of the garnet porphyroblast is homogeneous, with the highest pyrope and the lowest almandine components ($Alm_{50-52}Prp_{41-42}Grs_7Sps_1$) compared with other segments. The rim of the porphyroblastic garnet shows a sharp decrease in pyrope and grossular, compensated by an increase of almandine and spessartine.

Medium-grained garnet in the matrix is also chemically zoned. Its core ($Alm_{50-51}Prp_{41-42}Grs_{6-7}Sps_1$) contains high pyrope and relatively low almandine ($X_{Mg} = 0.43$–$0.45$), which is similar to the composition of the mantle part of the garnet porphyroblast (Figs 6 & 8b). The grossular content of garnet near the plagioclase corona surrounding quartz inclusions decreases sharply to 1–3 mol.% (Fig. 7b). The rim of the matrix garnet contains lower pyrope and higher almandine component, similar to the rim of porphyroblastic garnet (Fig. 8b). Additionally, the rim composition of the matrix garnet is correlated with the adjacent minerals. In cases without later symplectite,

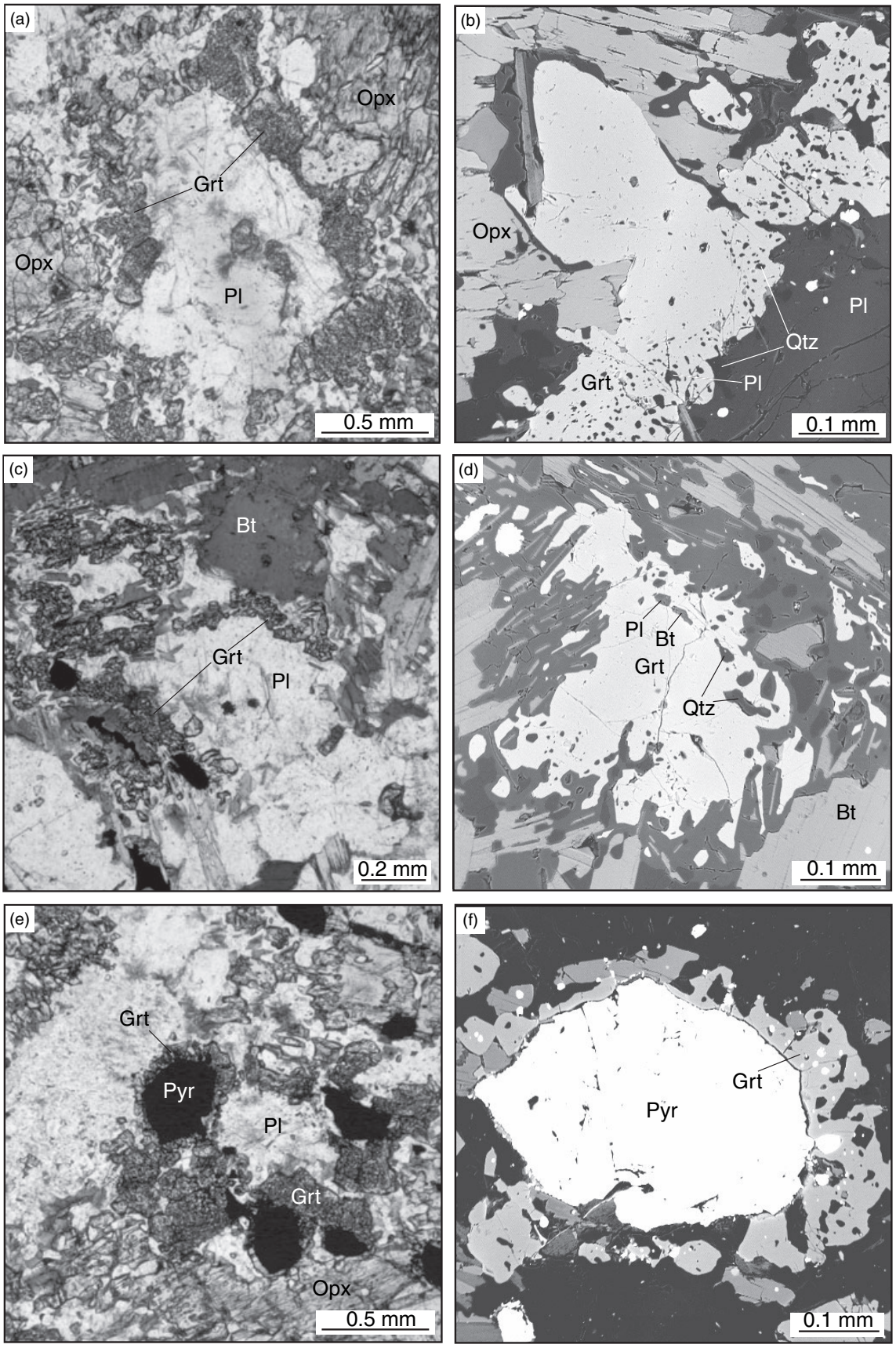

the garnet rim in contact with mafic phases is slightly richer in grossular ($Alm_{61-63}Prp_{33-36}Grs_{3-4}Spss_2$) than the garnet rim in contact with plagioclase ($Alm_{58-61}Prp_{36-37}Grs_{1-3}Spss_2$). Where the matrix garnet is partly replaced by later symplectites, its rim is enriched in almandine ($Alm_{64-68}Prp_{25-32}Grs_{3-5}Spss_2$) (Fig. 8b).

The fine-grained coronitic garnet shows slight compositional variation, which is clearly controlled by the composition of the nearby minerals (Fig. 6). The coronitic garnet surrounding orthopyroxene or biotite contains higher pyrope and lower almandine components ($Alm_{57-62}Prp_{34-38}Grs_{2-5}Spss_2$, $X_{Mg} = 0.35$–$0.40$) than that surrounding pyrite ($Alm_{64-65}Prp_{32-33}Grs_{2-3}Spss_2$, $X_{Mg} = 0.33$–$0.34$). Furthermore, the coronitic garnet is weakly zoned, its rim in contact with orthopyroxene and biotite contains lower grossular component (2–3 mol.%) than the rim in contact with plagioclase (4–5 mol.%). The garnet corona replaced by later symplectites is slightly rich in almandine and poor in pyrope ($Alm_{65-66}Prp_{30-31}Grs_{2-3}Sps_2$).

### Orthopyroxene

The four textural types of orthopyroxene recognized in the granulite exhibit significant variations in composition. (1) The matrix orthopyroxene is zoned in $Al^{VI}$ (core: 0.13–0.14 pfu; rim: 0.05–0.09 pfu). A slight rimward decrease of $X_{Mg}$ (0.61–0.65) was detected. Orthopyroxene rims near garnet coronae contain slightly lower $Al^{VI}$ (0.03–0.05 pfu) than rims without garnet coronae (Fig. 9). (2) Orthopyroxene included in the core of the matrix garnet has similar composition ($Al^{VI} = 0.12$–$0.14$ pfu, $X_{Mg} = 0.63$–$0.66$) to the core of the matrix orthopyroxene (Fig. 9). (3) Orthopyroxene included in the rim of the matrix garnet has low $Al^{VI}$ (0.06–0.08 pfu), which is similar to the rim of the matrix orthopyroxene away from garnet corona. (4) Fine-grained orthopyroxene in the symplectite shows large compositional variations in different reaction domains. Orthopyroxene in the symplectite after biotite contains lower $Al^{VI}$ (0.05–0.07 pfu) and $X_{Mg}$ (0.59–0.63) than that after garnet ($Al^{VI} = 0.08$–$0.12$ pfu, $X_{Mg} = 0.63$–$0.65$).

### Biotite

Representative compositions of biotite are listed in Table 3 and plotted in Fig. 10. The Ti content of biotite shows a negative correlation with $X_{Mg}$ (Fig. 10a), whereas the octahedrally coordinated Al shows a positive correlation with $X_{Mg}$ (Fig. 10b).

Six textural types of biotite are identified. (1) Biotite included in the core of the porphyroblastic garnet contains relatively low Ti (0.12–0.14 pfu) and $X_{Mg}$ (0.70–0.72), and high $Al^{VI}$ (0.29–0.31 pfu). (2) Medium-grained matrix biotite is homogeneous in $X_{Mg}$ (0.65–0.69) and Ti (0.21–0.26 pfu); however, biotite cores contain lower $Al^{VI}$ (0.11–0.15 pfu) than rims ($Al^{VI} = 0.15$–$0.22$ pfu) (Fig. 10b). (3) Biotite included in the core of the matrix garnet has the same composition to the core of the matrix biotite. (4) Biotite included in the coronitic garnet contains high $X_{Mg}$ (0.71–0.76) and relatively low Ti content (0.13–0.22 pfu). (5) The symplectitic biotite after garnet is rich in Ti (0.24–0.28 pfu), with $Al^{VI}$ content in the range 0.12–0.17 pfu. (6) The latest-stage biotite in the kelyphite replacing orthopyroxene has the lowest Ti content (0.05–0.07 pfu) and the highest $X_{Mg}$ (0.80–0.83) and $Al^{VI}$ (0.32–0.34 pfu).

### Feldspar

Eight textural types of plagioclase are identified. (1) Plagioclase included in the core of porphyroblastic garnet contains the highest anorthite component ($Ab_{39-47}An_{51-60}Or_{0-1}$). (2) Plagioclase included in the mantle of the porphyroblastic garnet is considerably more sodic ($Ab_{74}An_{24-25}Or_{0-1}$). (3) Medium-grained matrix plagioclase is slightly zoned (core: $Ab_{75-80}An_{20-21}Or_{1-4}$; rim: $Ab_{71-75}An_{23-28}Or_{0-1}$). Cores of coarser matrix plagioclase (> 2 mm) contain higher K ($Or_{3-4}$), but smaller plagioclase contains lower K ($Or_{1-2}$). (4) The plagioclase corona surrounding quartz included in the core of the matrix garnet has higher anorthite component ($An_{28-29}$) than the matrix plagioclase. (5) Plagioclase included in the coronitic garnet has a composition of $Ab_{78-80}An_{19-21}Or_{0-1}$. (6) Fine-grained plagioclase in the late symplectite is richer in anorthite ($An_{29-33}$) than the matrix plagioclase. (7) Plagioclase coexisting with later chlorite and muscovite is almost pure albite ($Ab_{97}$). (8) Plagioclase lamellae in the medium-grained matrix K-feldspar are pure albite.

The core of medium-grained matrix K-feldspar away from albite lamellae contains a higher albite component ($Or_{86-91}Ab_{9-13}An_{1-2}$) than that near albite lamellae ($Or_{96-99}Ab_{1-4}$); the lamellae-free rim of matrix K-feldspar contains also very low albite component ($Or_{95-98}Ab_{2-5}$).

### Cordierite

Cordierite only occurs in symplectite after garnet and biotite. $X_{Mg}$ varies from 0.80 to 0.83 (Table 5). The analysed oxide total is usually in the range of 98–

**Fig. 3.** Photomicrographs (a, c, e) and backscattered electron images (b, d, f) showing textures of coronitic garnet. (a) Garnet corona occurs between matrix plagioclase and orthopyroxene, sample HTL24. (b) Plagioclase near garnet corona contains abundant quartz inclusions, sample HTL24. (c) Garnet corona between matrix biotite and plagioclase, sample HTL19. (d) Garnet corona between biotite and plagioclase includes biotite, plagioclase and quartz, sample HTL13. (e) Garnet corona between matrix pyrite and plagioclase, sample HTL24. (f) Garnet corona around pyrite contains abundant quartz, sample HTL24.

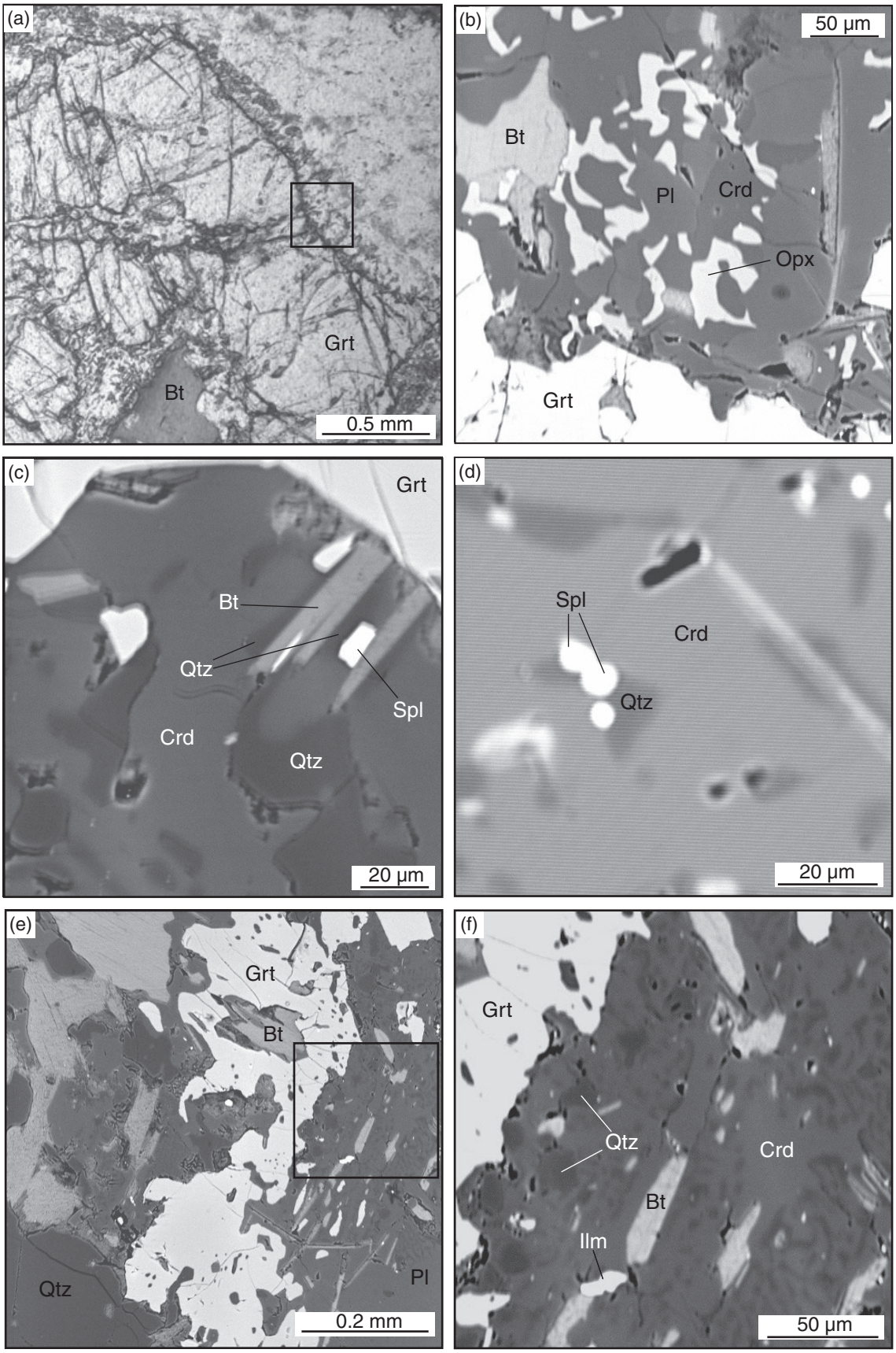

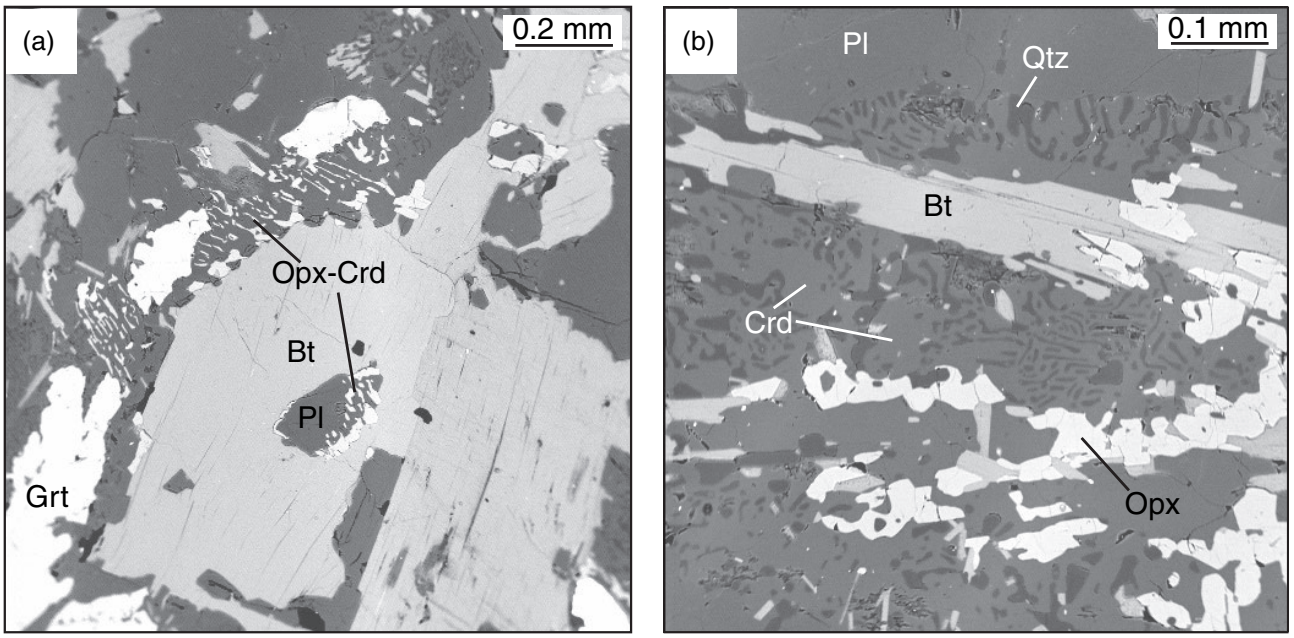


**Fig. 5.** Backscattered electron images showing symplectite after biotite. (a) Biotite replaced by Opx + Crd symplectite, sample HTL13. (b) Extensive replacement of biotite by Crd + Opx + Qtz symplectite, sample HTL19.

99 wt%, suggesting only minor amounts of $H_2O$ or $CO_2$.

### Amphibole

Amphibole compositions are recalculated following the recommendation of Dale *et al*. (2005) and classified following Leake *et al*. (1997). Amphibole only occurs in the core of porphyroblastic garnet. It is ferrotschermakitic amphibole with 1.8–2.0 pfu $Al^{VI}$, 0.38–0.41 $X_{Mg}$ [Mg/(Mg + Fe)], 0.40–0.42 pfu Na + K in A site and 0.20–0.24 pfu Na in M4 site.

### Spinel

There are two types of spinel identified. (1) Spinel associated with kyanite in the core of matrix plagioclase is a spinel–hercynite-gahnite–magnetite solid solution with $X_{Mg} = 0.35$–$0.36$. (2) The fine-grained spinel in the symplectite after garnet contains very high $Cr_2O_3$ (31–33 wt%) and its Cr/(Al + Cr) reaches 0.44–0.48. $X_{Mg}$ is very low (0.06–0.09).

## METAMORPHIC EVOLUTION AND *P–T* ESTIMATES

Based on the petrographical observations and mineral compositions described above, six metamorphic stages are inferred for the Huangtuling granulite. Textural and chemical data demonstrate that chemical disequilibrium is present among phases that formed in various stages and different reaction domains, chemical equilibrium is only reached in small specified reaction domains. This makes *P–T* calculations difficult. Mineral compositions in limited reaction domains where equilibrium is likely to have been achieved are used. Traditional thermobarometers are used for *P–T* calculations, together with THERMOCALC (v3.21, Powell *et al*., 1998), because the use of an internally consistent data set can enhance the accuracy of the magnitudes of differences in *P* and *T* of each stage. End-member activities of minerals are calculated using the AX program of Holland & Powell (1998).

### Stage I: amphibolite facies metamorphism

The earliest metamorphism is recorded by an amphibolite facies inclusion assemblage of amphibole (Amp1), muscovite (Ms1), biotite (Bt1), plagioclase (Pl1), ilmenite and quartz in the core of porphyroblastic garnet (Grt1). We interpret the innermost core of porphyroblastic garnet and the inclusion suite to be in chemical equilibrium, based on the following considerations: (1) compositions of both the innermost core of porphyroblastic garnet and the inclusion minerals fall in narrow ranges; (2) composition of the

**Fig. 4.** Photomicrographs (a) and backscattered electron images (b–f) showing symplectite after garnet. (a) Matrix garnet is replaced by fine-grained symplectite, sample HTL13. (b) Bt + Opx + Crd + Pl symplectite after garnet, sample HTL9a. (c) Symplectite of Bt (acicular grey grains) + Crd (grey) + Spl (bright) + Qtz (dark) after Grt (lighter grey), sample HTL13. Note Spl contacts with Qtz. (d) Spl coexisting with Qtz and Crd in the symplectite after garnet, sample HTL24. (e–f) Coronitic Grt around biotite is replaced by Crd + Bt + Ilm + Qtz symplectite, sample HTL19. The square in (e) shows area of (f).

**Table 1.** Representative compositions of garnet, formula unit based on 12 oxygen.

| Sample | 11a | 11a | 11a | 11a | 24 | 3 | 13 | 9a | 9a | 24 | 9a | 13 | 19 | 24 | 24 | 13 |
|---|---|---|---|---|---|---|---|---|---|---|---|---|---|---|---|---|
| Texture | P-core | P-core | P-mantle | P-rim | M-core | M-core | M-core near Pl | M-rim near Pl | M-rim near Bt | M-rim near Opx | M-rim near sym. | C-rim near Bt | C-rim near Pl | C-rim near Opx | C near Pyr | C near sym. |
| $SiO_2$ | 38.09 | 38.07 | 39.79 | 38.52 | 39.17 | 39.45 | 39.64 | 39.18 | 38.73 | 38.73 | 37.86 | 39.18 | 39.23 | 38.88 | 38.51 | 38.37 |
| $TiO_2$ | 0.11 | 0.03 | 0.00 | 0.02 | 0.01 | 0.05 | 0.00 | 0.04 | 0.03 | 0.00 | 0.17 | 0.04 | 0.02 | 0.04 | 0.00 | 0.01 |
| $Al_2O_3$ | 21.25 | 21.16 | 22.51 | 22.04 | 22.02 | 22.17 | 22.54 | 22.37 | 22.14 | 22.31 | 21.50 | 21.92 | 22.39 | 22.05 | 21.85 | 21.76 |
| $Cr_2O_3$ | 0.16 | 0.17 | 0.09 | 0.02 | 0.15 | 0.15 | 0.21 | 0.02 | 0.03 | 0.15 | 0.32 | 0.14 | 0.06 | 0.05 | 0.07 | 0.02 |
| FeO* | 29.80 | 29.55 | 24.11 | 28.24 | 24.08 | 24.23 | 25.25 | 27.64 | 28.63 | 27.80 | 30.40 | 27.08 | 27.86 | 27.08 | 29.16 | 29.51 |
| MnO | 1.02 | 0.94 | 0.24 | 0.81 | 0.37 | 0.48 | 0.48 | 0.75 | 0.91 | 0.81 | 1.12 | 0.76 | 0.80 | 0.68 | 0.82 | 1.13 |
| MgO | 5.64 | 5.41 | 11.32 | 8.46 | 10.64 | 10.87 | 11.19 | 9.50 | 8.11 | 8.42 | 6.42 | 9.78 | 8.70 | 9.50 | 8.12 | 7.62 |
| CaO | 4.01 | 4.26 | 2.26 | 1.24 | 2.80 | 2.62 | 1.27 | 0.78 | 1.41 | 1.41 | 1.47 | 1.49 | 1.81 | 1.41 | 0.81 | 0.95 |
| Total | 100.08 | 99.59 | 100.31 | 99.35 | 99.24 | 100.02 | 100.58 | 100.28 | 99.99 | 99.63 | 99.26 | 100.39 | 100.87 | 99.69 | 99.34 | 99.37 |
| Si | 2.995 | 3.007 | 3.001 | 2.996 | 2.998 | 2.996 | 2.993 | 3.000 | 2.999 | 2.997 | 2.991 | 2.998 | 2.998 | 2.995 | 3.005 | 3.004 |
| Ti | 0.007 | 0.002 | 0.000 | 0.001 | 0.001 | 0.003 | 0.000 | 0.002 | 0.002 | 0.000 | 0.010 | 0.002 | 0.001 | 0.002 | 0.000 | 0.001 |
| Al | 1.970 | 1.970 | 2.000 | 2.020 | 1.986 | 1.984 | 2.006 | 2.018 | 2.020 | 2.035 | 2.002 | 1.977 | 2.017 | 2.002 | 2.009 | 2.008 |
| Cr | 0.010 | 0.011 | 0.005 | 0.001 | 0.009 | 0.009 | 0.013 | 0.001 | 0.002 | 0.009 | 0.020 | 0.008 | 0.004 | 0.003 | 0.004 | 0.001 |
| Fe | 1.960 | 1.952 | 1.520 | 1.837 | 1.541 | 1.539 | 1.594 | 1.770 | 1.854 | 1.799 | 2.009 | 1.733 | 1.780 | 1.745 | 1.903 | 1.932 |
| Mn | 0.068 | 0.063 | 0.015 | 0.053 | 0.024 | 0.031 | 0.031 | 0.049 | 0.060 | 0.053 | 0.075 | 0.049 | 0.052 | 0.044 | 0.054 | 0.075 |
| Mg | 0.661 | 0.637 | 1.272 | 0.981 | 1.214 | 1.231 | 1.259 | 1.084 | 0.936 | 0.971 | 0.756 | 1.116 | 0.991 | 1.091 | 0.945 | 0.889 |
| Ca | 0.338 | 0.361 | 0.183 | 0.103 | 0.230 | 0.213 | 0.103 | 0.064 | 0.117 | 0.117 | 0.124 | 0.122 | 0.148 | 0.116 | 0.068 | 0.080 |
| $X_{Mg}$ | 0.252 | 0.246 | 0.456 | 0.348 | 0.441 | 0.444 | 0.441 | 0.380 | 0.336 | 0.351 | 0.273 | 0.392 | 0.358 | 0.385 | 0.332 | 0.315 |
| $X_{Alm}$ | 0.647 | 0.648 | 0.508 | 0.618 | 0.512 | 0.511 | 0.534 | 0.597 | 0.625 | 0.612 | 0.678 | 0.574 | 0.599 | 0.582 | 0.641 | 0.649 |
| $X_{Prp}$ | 0.218 | 0.211 | 0.425 | 0.330 | 0.403 | 0.408 | 0.422 | 0.365 | 0.316 | 0.330 | 0.255 | 0.369 | 0.334 | 0.364 | 0.318 | 0.299 |
| $X_{Grs}$ | 0.112 | 0.120 | 0.061 | 0.035 | 0.076 | 0.071 | 0.034 | 0.022 | 0.039 | 0.040 | 0.042 | 0.040 | 0.050 | 0.039 | 0.023 | 0.027 |
| $X_{Sps}$ | 0.022 | 0.021 | 0.005 | 0.018 | 0.008 | 0.010 | 0.010 | 0.016 | 0.020 | 0.018 | 0.025 | 0.016 | 0.017 | 0.015 | 0.018 | 0.025 |

FeO*, all Fe as FeO; $X_{Mg} = Mg/(Mg + Fe)$; P, porphyroblast (cm size); M, matrix (mm size); C, corona; sym., symplectite.

**Table 2.** Representative compositions of orthopyroxene, formula unit based on 6 oxygen.

| Sample no. | 3 | 9a | 11a | 19 | 9a | 9a | 24 | 19 | 24 | 3 | 9a | 11a | 13 |
|---|---|---|---|---|---|---|---|---|---|---|---|---|---|
| Texture | M-core | M-core | in core of M Grt | in core of M Grt | M-rim near Bt | M-rim near Grt | in rim of M Grt | M-rim near Grt C | M-rim near Grt C | sym. after Bt | sym. after Bt | sym. after Grt | sym. after Grt |
| $SiO_2$ | 49.88 | 50.56 | 49.97 | 49.77 | 49.97 | 51.42 | 51.67 | 51.20 | 51.42 | 51.50 | 51.87 | 51.98 | 51.79 |
| $TiO_2$ | 0.10 | 0.12 | 0.05 | 0.10 | 0.05 | 0.05 | 0.10 | 0.02 | 0.08 | 0.08 | 0.14 | 0.07 | 0.01 |
| $Al_2O_3$ | 6.05 | 6.23 | 6.05 | 6.24 | 6.05 | 3.52 | 3.00 | 3.02 | 2.51 | 3.02 | 2.62 | 3.67 | 3.93 |
| $Cr_2O_3$ | 0.10 | 0.07 | 0.06 | 0.09 | 0.06 | 0.03 | 0.04 | 0.00 | 0.03 | 0.15 | 0.13 | 0.12 | 0.10 |
| FeO* | 22.03 | 22.13 | 22.00 | 21.99 | 22.00 | 24.19 | 23.62 | 24.18 | 23.92 | 22.34 | 23.85 | 22.35 | 21.91 |
| MnO | 0.18 | 0.16 | 0.15 | 0.27 | 0.15 | 0.19 | 0.29 | 0.08 | 0.24 | 0.17 | 0.25 | 0.20 | 0.19 |
| MgO | 20.51 | 21.13 | 20.96 | 21.21 | 20.96 | 21.04 | 21.99 | 21.54 | 21.43 | 21.75 | 21.05 | 21.54 | 21.17 |
| CaO | 0.05 | 0.07 | 0.06 | 0.21 | 0.06 | 0.05 | 0.07 | 0.05 | 0.05 | 0.05 | 0.11 | 0.10 | 0.08 |
| $Na_2O$ | 0.02 | 0.01 | 0.00 | 0.00 | 0.00 | 0.00 | 0.02 | 0.02 | 0.00 | 0.01 | 0.03 | 0.00 | 0.01 |
| $K_2O$ | 0.11 | 0.00 | 0.01 | 0.00 | 0.01 | 0.00 | 0.00 | 0.00 | 0.01 | 0.00 | 0.02 | 0.01 | 0.00 |
| NiO | 0.00 | 0.04 | 0.03 | 0.00 | 0.03 | 0.02 | 0.01 | 0.00 | 0.03 | 0.04 | 0.00 | 0.00 | 0.02 |
| Total | 99.03 | 100.52 | 99.34 | 99.88 | 99.34 | 100.51 | 100.81 | 100.12 | 99.71 | 99.11 | 100.07 | 100.04 | 99.21 |
| Si | 1.870 | 1.865 | 1.866 | 1.851 | 1.866 | 1.916 | 1.917 | 1.917 | 1.932 | 1.931 | 1.940 | 1.928 | 1.932 |
| Ti | 0.003 | 0.003 | 0.001 | 0.003 | 0.001 | 0.001 | 0.003 | 0.001 | 0.002 | 0.002 | 0.004 | 0.002 | 0.000 |
| $Al^{IV}$ | 0.130 | 0.135 | 0.134 | 0.149 | 0.134 | 0.084 | 0.083 | 0.083 | 0.068 | 0.069 | 0.060 | 0.072 | 0.068 |
| $Al^{VI}$ | 0.138 | 0.136 | 0.133 | 0.125 | 0.133 | 0.071 | 0.048 | 0.050 | 0.043 | 0.065 | 0.055 | 0.088 | 0.105 |
| Cr | 0.003 | 0.002 | 0.002 | 0.003 | 0.002 | 0.001 | 0.001 | 0.000 | 0.001 | 0.004 | 0.004 | 0.004 | 0.003 |
| Fe | 0.691 | 0.683 | 0.687 | 0.684 | 0.687 | 0.754 | 0.733 | 0.757 | 0.752 | 0.701 | 0.746 | 0.693 | 0.684 |
| Mn | 0.006 | 0.005 | 0.005 | 0.009 | 0.005 | 0.006 | 0.009 | 0.003 | 0.008 | 0.005 | 0.008 | 0.006 | 0.006 |
| Mg | 1.147 | 1.162 | 1.167 | 1.176 | 1.167 | 1.169 | 1.216 | 1.202 | 1.201 | 1.216 | 1.174 | 1.191 | 1.177 |
| Ca | 0.002 | 0.003 | 0.002 | 0.008 | 0.002 | 0.002 | 0.003 | 0.002 | 0.002 | 0.002 | 0.004 | 0.004 | 0.003 |
| Na | 0.002 | 0.001 | 0.000 | 0.000 | 0.000 | 0.000 | 0.001 | 0.002 | 0.000 | 0.001 | 0.002 | 0.000 | 0.001 |
| K | 0.005 | 0.000 | 0.000 | 0.000 | 0.000 | 0.000 | 0.000 | 0.000 | 0.000 | 0.000 | 0.001 | 0.000 | 0.000 |
| Ni | 0.000 | 0.001 | 0.001 | 0.000 | 0.001 | 0.001 | 0.000 | 0.000 | 0.001 | 0.001 | 0.000 | 0.000 | 0.001 |
| $X_{Mg}$ | 0.624 | 0.630 | 0.629 | 0.632 | 0.629 | 0.608 | 0.624 | 0.614 | 0.615 | 0.634 | 0.611 | 0.632 | 0.633 |

FeO*, all Fe as FeO; $X_{Mg} = Mg/(Mg + Fe)$; M, matrix; C, corona; sym., symplectite.

innermost garnet core is distinct from other garnet segments; (3) compositions of biotite and plagioclase inclusions are distinct from those in the matrix; (4) line traverses (200–300 $\mu$m) on garnet near biotite and plagioclase inclusions do not show any clear chemical zoning, and thus rule out later diffusional Fe–Mg exchange between garnet host and inclusions. Therefore, the mineral assemblage of the initial amphibolite facies stage can be constrained to be Grt1 + Ms1 + Bt1 + Pl1 + Amp1 + Ilm + Qtz.

The following three equilibria describe reactions among end-members of equilibrium garnet, biotite, plagioclase and quartz in stage I:

$$\mathrm{Pyr} + \mathrm{Ann} = \mathrm{Alm} + \mathrm{Phl(GB)};$$

$$\mathrm{Prp} + 2\mathrm{Grs} + 3\mathrm{East} + 6\mathrm{Qtz} = 3\mathrm{Phl} + 6\mathrm{An(GBPQ\text{-}1)};$$

**Table 3.** Representative compositions of biotite, formula unit based on 11 oxygen.

| Sample | 11a | 11a | 11a | 24 | 13 | 19 | 9a | 24 | 13 | 19 | 9a | 13 | 19 | 1 |
|---|---|---|---|---|---|---|---|---|---|---|---|---|---|---|
| Texture | in core of Grt P | in core of Grt P | in core of M Grt | in core of M Grt | M-core | M-core | M-rim | M-rim | in Grt C | in Grt C | sym. | sym. | sym. | kely -Opx-rim |
| $SiO_2$ | 36.73 | 36.93 | 36.60 | 36.97 | 37.03 | 36.57 | 37.12 | 36.54 | 36.95 | 37.17 | 36.85 | 36.86 | 36.65 | 38.55 |
| $TiO_2$ | 2.58 | 2.08 | 4.49 | 4.05 | 4.16 | 4.59 | 3.70 | 4.05 | 3.42 | 3.13 | 4.62 | 5.08 | 5.04 | 1.23 |
| $Al_2O_3$ | 18.09 | 17.89 | 15.60 | 16.56 | 15.81 | 15.88 | 16.86 | 16.63 | 16.90 | 16.93 | 16.88 | 16.00 | 15.67 | 18.29 |
| $Cr_2O_3$ | 0.22 | 0.12 | 0.72 | 1.94 | 0.78 | 0.72 | 0.45 | 0.38 | 0.46 | 0.71 | 0.52 | 0.72 | 0.68 | 0.35 |
| FeO* | 11.61 | 11.01 | 13.70 | 12.28 | 13.16 | 13.48 | 12.83 | 12.39 | 11.52 | 11.32 | 12.11 | 12.75 | 12.71 | 8.53 |
| MnO | 0.00 | 0.00 | 0.05 | 0.06 | 0.04 | 0.04 | 0.03 | 0.06 | 0.01 | 0.11 | 0.00 | 0.05 | 0.00 | 0.03 |
| MgO | 15.33 | 15.53 | 14.01 | 14.75 | 14.60 | 14.58 | 14.98 | 15.51 | 16.13 | 16.62 | 14.95 | 14.16 | 14.13 | 19.15 |
| CaO | 0.04 | 0.04 | 0.03 | 0.15 | 0.08 | 0.02 | 0.00 | 0.00 | 0.05 | 0.09 | 0.04 | 0.00 | 0.02 | 0.05 |
| $Na_2O$ | 0.17 | 0.17 | 0.22 | 0.35 | 0.20 | 0.20 | 0.26 | 0.24 | 0.37 | 0.33 | 0.25 | 0.29 | 0.28 | 0.22 |
| $K_2O$ | 10.32 | 10.32 | 8.83 | 8.28 | 8.55 | 8.92 | 8.48 | 8.49 | 9.54 | 9.45 | 8.96 | 9.25 | 9.04 | 8.07 |
| NiO | 0.06 | 0.06 | 0.06 | 0.12 | 0.10 | 0.07 | 0.07 | 0.14 | 0.09 | 0.03 | 0.07 | 0.12 | 0.06 | 0.05 |
| Total | 95.15 | 94.15 | 94.32 | 95.49 | 94.49 | 95.06 | 94.79 | 94.41 | 95.45 | 95.88 | 95.25 | 95.27 | 94.30 | 94.52 |
| Si | 2.712 | 2.746 | 2.744 | 2.715 | 2.756 | 2.719 | 2.741 | 2.710 | 2.714 | 2.715 | 2.710 | 2.729 | 2.739 | 2.774 |
| Ti | 0.143 | 0.116 | 0.253 | 0.223 | 0.233 | 0.256 | 0.205 | 0.226 | 0.189 | 0.172 | 0.256 | 0.283 | 0.283 | 0.067 |
| $Al^{IV}$ | 1.288 | 1.254 | 1.256 | 1.285 | 1.244 | 1.281 | 1.259 | 1.290 | 1.286 | 1.285 | 1.290 | 1.271 | 1.261 | 1.226 |
| $Al^{VI}$ | 0.286 | 0.313 | 0.123 | 0.148 | 0.143 | 0.110 | 0.209 | 0.163 | 0.178 | 0.172 | 0.173 | 0.125 | 0.119 | 0.325 |
| Cr | 0.013 | 0.007 | 0.043 | 0.112 | 0.046 | 0.042 | 0.026 | 0.023 | 0.027 | 0.041 | 0.030 | 0.042 | 0.040 | 0.020 |
| Fe | 0.717 | 0.685 | 0.859 | 0.754 | 0.819 | 0.838 | 0.792 | 0.768 | 0.708 | 0.691 | 0.745 | 0.789 | 0.794 | 0.513 |
| Mn | 0.000 | 0.000 | 0.003 | 0.004 | 0.003 | 0.002 | 0.002 | 0.004 | 0.001 | 0.007 | 0.000 | 0.003 | 0.000 | 0.002 |
| Mg | 1.688 | 1.721 | 1.566 | 1.615 | 1.620 | 1.615 | 1.649 | 1.715 | 1.766 | 1.809 | 1.639 | 1.562 | 1.574 | 2.054 |
| Ca | 0.003 | 0.003 | 0.003 | 0.012 | 0.006 | 0.002 | 0.000 | 0.000 | 0.004 | 0.007 | 0.003 | 0.000 | 0.002 | 0.004 |
| Na | 0.025 | 0.025 | 0.032 | 0.050 | 0.028 | 0.028 | 0.038 | 0.034 | 0.053 | 0.047 | 0.036 | 0.042 | 0.040 | 0.031 |
| K | 0.972 | 0.979 | 0.845 | 0.775 | 0.812 | 0.846 | 0.799 | 0.803 | 0.894 | 0.881 | 0.840 | 0.873 | 0.862 | 0.741 |
| Ni | 0.000 | 0.000 | 0.000 | 0.000 | 0.000 | 0.000 | 0.000 | 0.000 | 0.000 | 0.000 | 0.000 | 0.000 | 0.000 | 0.000 |
| $X_{Mg}$ | 0.702 | 0.715 | 0.646 | 0.682 | 0.664 | 0.658 | 0.675 | 0.691 | 0.714 | 0.723 | 0.688 | 0.664 | 0.665 | 0.800 |

FeO*, all Fe as FeO; $X_{Mg} = Mg/(Mg + Fe)$; P, porphyroblast; M, matrix; C, corona; sym., symplectite; kely., kelyphite.

**Table 4.** Representative compositions of plagioclase, formula unit based on 8 oxygen.

| Sample | 11a | 11a | 11a | 19 | 24 | 19 | 24 | 24 | 19 | 3 | 11a | 1 | 19 | 19 |
|---|---|---|---|---|---|---|---|---|---|---|---|---|---|---|
| Mineral | Pl | Pl | Pl | Pl | Pl | Pl | Pl | Pl | Pl | Pl | Pl | Pl | Kfs | Kfs |
| Texture | in core of Grt P | in core of Grt P | in mantle of Grt P | M-core | M-core | M-rim near Grt | in core of M Grt | in Grt C | in Grt C | sym. | sym. | kely. | M-core | M-rim |
| $SiO_2$ | 54.89 | 54.27 | 62.41 | 63.39 | 63.49 | 61.10 | 61.66 | 63.00 | 63.49 | 61.13 | 59.41 | 67.14 | 65.25 | 64.34 |
| $TiO_2$ | 0.05 | 0.05 | 0.12 | 0.04 | 0.06 | 0.01 | 0.00 | 0.03 | 0.06 | 0.03 | 0.00 | 0.01 | 0.07 | 0.03 |
| $Al_2O_3$ | 28.60 | 29.66 | 23.91 | 23.45 | 23.51 | 24.55 | 24.56 | 23.60 | 23.51 | 24.80 | 25.18 | 20.57 | 18.94 | 18.50 |
| $Cr_2O_3$ | 0.00 | 0.02 | 0.00 | 0.00 | 0.00 | 0.02 | 0.00 | 0.00 | 0.00 | 0.00 | 0.03 | 0.00 | 0.00 | 0.00 |
| FeO* | 0.38 | 0.02 | 0.06 | 0.02 | 0.00 | 0.12 | 0.10 | 0.00 | 0.00 | 0.00 | 0.14 | 0.04 | 0.00 | 0.07 |
| MnO | 0.00 | 0.02 | 0.11 | 0.00 | 0.00 | 0.00 | 0.00 | 0.00 | 0.00 | 0.00 | 0.06 | 0.00 | 0.00 | 0.00 |
| MgO | 0.00 | 0.01 | 0.00 | 0.00 | 0.00 | 0.04 | 0.01 | 0.00 | 0.00 | 0.00 | 0.01 | 0.00 | 0.00 | 0.01 |
| CaO | 10.62 | 11.78 | 5.09 | 4.36 | 4.36 | 5.82 | 5.87 | 4.47 | 4.36 | 6.20 | 6.75 | 0.68 | 0.40 | 0.00 |
| $Na_2O$ | 5.44 | 4.94 | 8.77 | 8.90 | 8.80 | 8.27 | 8.39 | 9.10 | 9.20 | 8.20 | 7.70 | 11.05 | 1.30 | 0.46 |
| $K_2O$ | 0.18 | 0.17 | 0.32 | 0.61 | 0.63 | 0.13 | 0.09 | 0.04 | 0.13 | 0.15 | 0.05 | 0.02 | 14.81 | 16.01 |
| Total | 100.15 | 100.94 | 100.79 | 100.77 | 100.84 | 100.05 | 100.68 | 100.23 | 100.74 | 100.51 | 99.35 | 99.51 | 100.76 | 99.42 |
| Si | 2.473 | 2.430 | 2.750 | 2.786 | 2.787 | 2.714 | 2.721 | 2.778 | 2.786 | 2.704 | 2.666 | 2.949 | 2.979 | 2.990 |
| Ti | 0.002 | 0.002 | 0.004 | 0.001 | 0.002 | 0.000 | 0.000 | 0.001 | 0.002 | 0.001 | 0.000 | 0.000 | 0.002 | 0.001 |
| Al | 1.519 | 1.565 | 1.241 | 1.215 | 1.216 | 1.285 | 1.277 | 1.227 | 1.216 | 1.293 | 1.331 | 1.065 | 1.019 | 1.013 |
| Cr | 0.000 | 0.001 | 0.000 | 0.000 | 0.000 | 0.001 | 0.000 | 0.000 | 0.000 | 0.000 | 0.001 | 0.000 | 0.000 | 0.000 |
| Fe | 0.014 | 0.001 | 0.002 | 0.001 | 0.000 | 0.004 | 0.004 | 0.000 | 0.000 | 0.000 | 0.005 | 0.001 | 0.000 | 0.003 |
| Mn | 0.000 | 0.001 | 0.004 | 0.000 | 0.000 | 0.000 | 0.000 | 0.000 | 0.000 | 0.000 | 0.002 | 0.000 | 0.000 | 0.000 |
| Mg | 0.000 | 0.001 | 0.000 | 0.000 | 0.000 | 0.003 | 0.000 | 0.000 | 0.000 | 0.000 | 0.000 | 0.000 | 0.000 | 0.001 |
| Ca | 0.513 | 0.565 | 0.240 | 0.205 | 0.205 | 0.277 | 0.277 | 0.211 | 0.205 | 0.294 | 0.325 | 0.032 | 0.020 | 0.000 |
| Na | 0.476 | 0.429 | 0.749 | 0.758 | 0.749 | 0.712 | 0.718 | 0.778 | 0.783 | 0.703 | 0.670 | 0.941 | 0.115 | 0.042 |
| K | 0.010 | 0.010 | 0.018 | 0.034 | 0.035 | 0.007 | 0.005 | 0.002 | 0.007 | 0.008 | 0.003 | 0.001 | 0.862 | 0.949 |
| $X_{an}$ | 0.513 | 0.563 | 0.239 | 0.206 | 0.207 | 0.278 | 0.277 | 0.213 | 0.206 | 0.292 | 0.325 | 0.033 | 0.020 | 0.000 |
| $X_{ab}$ | 0.476 | 0.427 | 0.744 | 0.760 | 0.757 | 0.715 | 0.718 | 0.785 | 0.787 | 0.700 | 0.672 | 0.966 | 0.115 | 0.042 |
| $X_{or}$ | 0.010 | 0.010 | 0.018 | 0.034 | 0.036 | 0.007 | 0.005 | 0.002 | 0.007 | 0.008 | 0.003 | 0.001 | 0.865 | 0.958 |

FeO*, all Fe as FeO; P, porphyroblast; M, matrix; C, corona; sym., symplectite; kely., kelyphite.

and,

$$\mathrm{Alm} + 2\mathrm{Grs} + 3\mathrm{East} + 6\mathrm{Qtz} = 2\mathrm{Phl} + \mathrm{Ann} + 6\mathrm{An}\ (\mathrm{GBPQ\text{-}2}).$$

Compositions of Bt1 and Pl1 inclusions in the innermost core of the porphyroblastic garnet and the host Grt1 in samples HTL11a and HTL24 were used to estimate *P–T* conditions of stage I. Using THERMOCALC and the three end-member reactions gives results of 520–550 °C and 6.3–7.0 kbar (Fig. 11). The Grt–Bt thermometer of Holdaway (2000) with the Grt–Bt–Pl–Qtz baro-

**Table 5.** Representative compositions of muscovite, amphibole, chlorite and cordierite.

| Sample | 11a | 11a | 3 | 24 | 13 | 19 | 1 | 1 |
|---|---|---|---|---|---|---|---|---|
| Mineral | Ms | Amp | Crd | Crd | Crd | Crd | Ms | Chl |
| Texture | in core of Grt P | in core of Grt P | sym. after Grt | sym. after Grt | sym. after Bt | sym. after Bt | kely. | kely. |
| $SiO_2$ | 47.39 | 41.34 | 49.47 | 49.04 | 49.86 | 48.79 | 46.64 | 27.43 |
| $TiO_2$ | 0.06 | 0.41 | 0.00 | 0.00 | 0.00 | 0.05 | 0.09 | 0.12 |
| $Al_2O_3$ | 32.79 | 13.11 | 34.92 | 34.35 | 34.09 | 34.19 | 31.01 | 17.14 |
| $Cr_2O_3$ | 0.04 | 0.00 | 0.01 | 0.02 | 0.00 | 0.01 | 0.00 | 0.05 |
| FeO* | 1.77 | 21.43.43 | 4.17 | 4.16 | 4.51 | 4.75 | 3.40 | 25.08 |
| MnO | 0.02 | 0.05 | 0.02 | 0.05 | 0.07 | 0.00 | 0.04 | 0.07 |
| MgO | 0.36 | 8.47 | 9.89 | 10.98 | 10.01 | 10.62 | 3.80 | 15.44 |
| CaO | 3.63 | 10.3 | 0.05 | 0.00 | 0.12 | 0.04 | 0.09 | 0.06 |
| $Na_2O$ | 0.81 | 1.91 | 0.11 | 0.10 | 0.07 | 0.10 | 0.14 | 0.13 |
| $K_2O$ | 7.56 | 0.43 | 0.05 | 0.00 | 0.02 | 0.03 | 9.85 | 0.14 |
| NiO | 0.00 | 0.00 | 0.00 | 0.03 | 0.02 | 0.03 | 0.03 | 0.00 |
| Total | 94.42 | 97.45 | 98.70 | 98.72 | 98.77 | 98.60 | 95.08 | 85.64 |
| O | 11 | 23 | 18 | 18 | 18 | 18 | 11 | 28 |
| Si | 3.171 | 6.329 | 4.982 | 4.921 | 5.027 | 4.914 | 3.141 | 2.961 |
| Ti | 0.003 | 0.047 | 0.000 | 0.000 | 0.000 | 0.004 | 0.005 | 0.010 |
| Al | 2.590 | 3.366 | 4.145 | 4.061 | 4.051 | 4.058 | 2.460 | 2.180 |
| Cr | 0.002 | 0.000 | 0.001 | 0.002 | 0.000 | 0.001 | 0.000 | 0.004 |
| Fe | 0.099 | 2.744 | 0.352 | 0.349 | 0.381 | 0.400 | 0.192 | 2.264 |
| Mn | 0.001 | 0.006 | 0.001 | 0.005 | 0.006 | 0.000 | 0.002 | 0.006 |
| Mg | 0.036 | 1.933 | 1.485 | 1.642 | 1.505 | 1.594 | 0.381 | 2.483 |
| Ca | 0.260 | 1.690 | 0.005 | 0.000 | 0.013 | 0.005 | 0.006 | 0.007 |
| Na | 0.105 | 0.567 | 0.022 | 0.018 | 0.014 | 0.019 | 0.018 | 0.027 |
| K | 0.645 | 0.084 | 0.007 | 0.000 | 0.003 | 0.003 | 0.846 | 0.019 |
| Ni | 0.000 | 0.000 | 0.000 | 0.002 | 0.002 | 0.002 | 0.000 | 0.000 |
| $X_{Mg}$ | 0.268 | 0.413 | 0.809 | 0.825 | 0.798 | 0.799 | 0.665 | 0.523 |
| Na(A) | | 0.317 | | | | | | |
| Na(M4) | | 0.236 | | | | | | |

FeO*, all Fe as FeO; $X_{Mg}$ = Mg/(Mg + Fe); P, porphyroblast; sym., symplectite; kely., kelyphite.

**Table 6.** Representative compositions of spinel, formula unit based on 4 oxygen.

| Sample | 24 | 11a | 3 | 9a | 9a | 24 | 24 |
|---|---|---|---|---|---|---|---|
| Texture | in core of M Pl | n core of M Grt | sym. | sym. | sym. | sym. | sym. |
| $SiO_2$ | 0.01 | 0.05 | 0.18 | 0.44 | 1.16 | 0.17 | 0.14 |
| $TiO_2$ | 0.08 | 0.18 | 0.50 | 0.45 | 0.46 | 0.55 | 0.12 |
| $Al_2O_3$ | 60.76 | 60.68 | 26.10 | 26.74 | 24.39 | 24.79 | 26.20 |
| $Cr_2O_3$ | 0.02 | 0.03 | 32.97 | 31.79 | 33.30 | 32.92 | 33.23 |
| FeO* | 28.03 | 28.57 | 34.61 | 33.99 | 34.44 | 35.27 | 34.84 |
| MnO | 0.08 | 0.04 | 0.24 | 0.17 | 0.20 | 0.19 | 0.15 |
| MgO | 8.64 | 8.59 | 1.66 | 1.71 | 1.58 | 1.35 | 1.84 |
| NiO | 0.19 | 0.19 | 0.22 | 0.17 | 0.21 | 0.20 | 0.02 |
| ZnO | 1.62 | 1.86 | 3.42 | 3.81 | 3.06 | 3.91 | 3.59 |
| Total | 99.44 | 100.20 | 99.90 | 99.27 | 98.79 | 99.34 | 100.12 |
| Si | 0.000 | 0.001 | 0.006 | 0.014 | 0.039 | 0.006 | 0.005 |
| Ti | 0.002 | 0.004 | 0.012 | 0.011 | 0.011 | 0.014 | 0.003 |
| Al | 1.963 | 1.951 | 1.006 | 1.033 | 0.955 | 0.968 | 1.006 |
| Cr | 0.001 | 0.001 | 0.853 | 0.824 | 0.874 | 0.862 | 0.856 |
| Fe | 0.643 | 0.652 | 0.947 | 0.932 | 0.956 | 0.977 | 0.950 |
| Mn | 0.002 | 0.001 | 0.007 | 0.005 | 0.006 | 0.005 | 0.004 |
| Mg | 0.353 | 0.349 | 0.081 | 0.084 | 0.078 | 0.067 | 0.089 |
| Ni | 0.004 | 0.004 | 0.006 | 0.004 | 0.006 | 0.005 | 0.000 |
| Zn | 0.033 | 0.037 | 0.083 | 0.092 | 0.075 | 0.096 | 0.086 |
| Cr/(Al + Cr) | 0.000 | 0.000 | 0.459 | 0.444 | 0.478 | 0.471 | 0.460 |
| $X_{Mg}$ | 0.355 | 0.349 | 0.079 | 0.082 | 0.076 | 0.064 | 0.086 |

FeO*, all Fe as FeO; $X_{Mg}$ = Mg/(Mg + Fe); M, matrix; sym., symplectite.

meter of Wu *et al.* (2004) yield similar temperature and pressure results of 570–600 °C and 6.2–6.9 kbar.

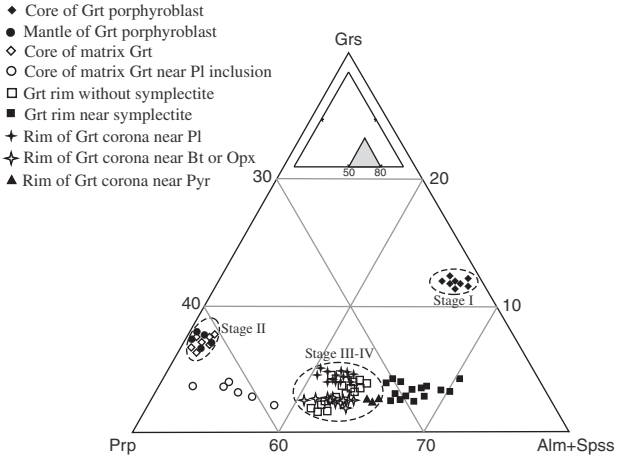


**Fig. 6.** Ternary grossular–pyrope–(spessartine + almandine) diagram of various garnet types from the granulites.

## Stage II: High-pressure/high-temperature granulite facies metamorphism

The second stage of metamorphism is characterized by growth of the garnet porphyroblast mantle (hereafter referred as Grt2a) and minerals included in this zone (Pl2a, Bt2a, Opx2a, Rut, Qtz), which are distinct both in assemblage and in compositions from those in the core of the garnet porphyroblast (Grt1). The core of the medium-grained matrix garnet (Grt2b) is similar in composition to the mantle of garnet porphyroblast (Grt2a), and compositions of the core of medium-grained matrix biotite (Bt2b) and plagioclase (Pl2b) are also similar to those included in the mantle of porphyroblastic garnet (Grt2a). These features are used to infer that the cores of medium-grained garnet (Grt2b), biotite (Bt2b), plagioclase (Pl2b), quartz, and included minerals (kyanite, rutile and plagioclase) are in equilibrium with the mantle of garnet porphyroblast (Grt2a). Additionally, the core of the matrix orthopyroxene (Opx2) is similar in composition to the fine-grained orthopyroxene included in the core of the matrix garnet (Grt2b), suggesting that they also formed in this stage. Therefore, the equilibrium assemblage for stage II is inferred to be Grt2 + Opx2 + Bt2 + Pl2 + Kfs + Ky + Ru + Qtz.

From the initial amphibolite facies stage to the high-pressure granulite facies stage, muscovite, amphibole and ilmenite became unstable and neoblastic orthopyroxene, kyanite, K-feldspar and rutile are produced. Although garnet, biotite and plagioclase are stable in both stages, their compositions are distinct. Based on the above consideration, biotite breakdown reactions probably took place during stage II. Biotite breakdown reactions have been experimentally investigated by Vielzeuf & Montel (1994), Patiño Douce & Beard (1995) and Stevens *et al.* (1997) (Fig. 12). These experiments indicate that (1) orthopyroxene forms

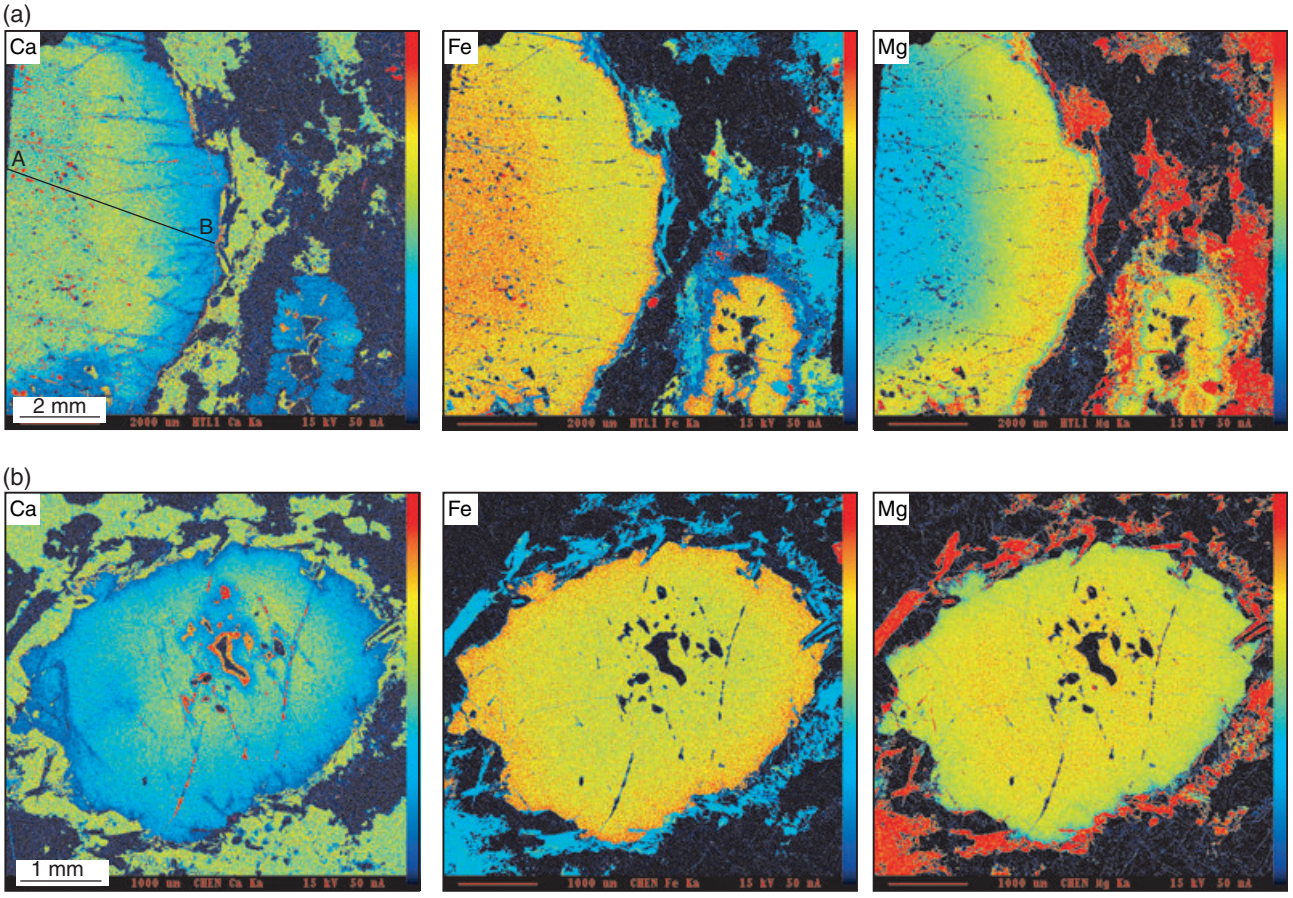


**Fig. 7.** (a) Ca, Fe and Mg X-ray maps of porphyroblastic garnet; line A–B is the traverse in Fig. 8. (b) Ca, Fe and Mg X-ray maps of a medium-grained garnet in the matrix. Note the plagioclase around quartz included in the garnet core.

(Opx-in) at 900–930 °C at 10–15 kbar; (2) high-Ti biotite and orthopyroxene coexist up to 930–970 °C at 10–15 kbar; and (3) biotite is unstable (Bt-out) at higher temperatures (Fig. 12). In stage II, orthopyroxene and high-Ti biotite are in texturally equilibrium, which indicates that the *P–T* conditions of stage II must be located in between the Opx-in and Bt-out curves (Fig. 12).

Core compositions of medium-grained matrix garnet (Grt2b), orthopyroxene (Opx2b), plagioclase (Pl2b), and compositions of mineral inclusions in these phases were used for *P–T* calculations of stage II. The matrix biotite shows weak zonation in $Al^{VI}$, however, its Fe and Mg contents are constant, indicating that the composition of biotite might be reset by retrograde diffusional exchange (Spear, 1993). Therefore, biotite is not used for *P–T* estimation.

The following equilibria describe end-member reactions among the equilibrium assemblage of garnet, orthopyroxene, plagioclase and quartz:

$$2\mathrm{Prp} + 3\mathrm{Fs} = 2\mathrm{Alm} + 3\mathrm{En}(\mathrm{GO});$$

$$2\mathrm{Prp} + \mathrm{Grs} + 3\mathrm{Qtz} = 3\mathrm{En} + 3\mathrm{An}(\mathrm{GOPQ\text{-}1});$$

and

$$2\mathrm{Alm} + \mathrm{Grs} + 3\mathrm{Qtz} = 3\mathrm{Fs} + 3\mathrm{An}(\mathrm{GOPQ\text{-}2});$$

$$\mathrm{Grs} + 2\mathrm{Ky} + \mathrm{Qtz} = 3\mathrm{An}(\mathrm{GASP}).$$

Calculations on the above end-member reactions in THERMOCALC give results of 920–980 °C and 12.0–15.5 kbar (Fig. 11). For comparison, the Grt–Opx thermometers of Harley (1984) and Bhattacharya *et al.* (1991) combined with the Grt–Opx–Pl–Qtz barometer of Newton & Perkins (1982) and the Grt–Ky–Pl–Qtz barometer of Holdaway (2001) give 930–960 °C and 13.3–16.3 kbar, which are consistent with the THERMOCALC results. Calculated temperatures are consistent with the inference of Opx-in $< T <$ Bt-out.

### Stage III: cooling and decompression

The rims of porphyroblastic garnet, medium-grained matrix garnet (Grt3), orthopyroxene (Opx3), plagioclase (Pl3) and biotite (Bt3) show systematic retrograde zoning. Compared with the high Mg and Ca garnet in stage II, the rims of porphyroblastic garnet and medium-grained matrix garnet (Grt3) contain much higher

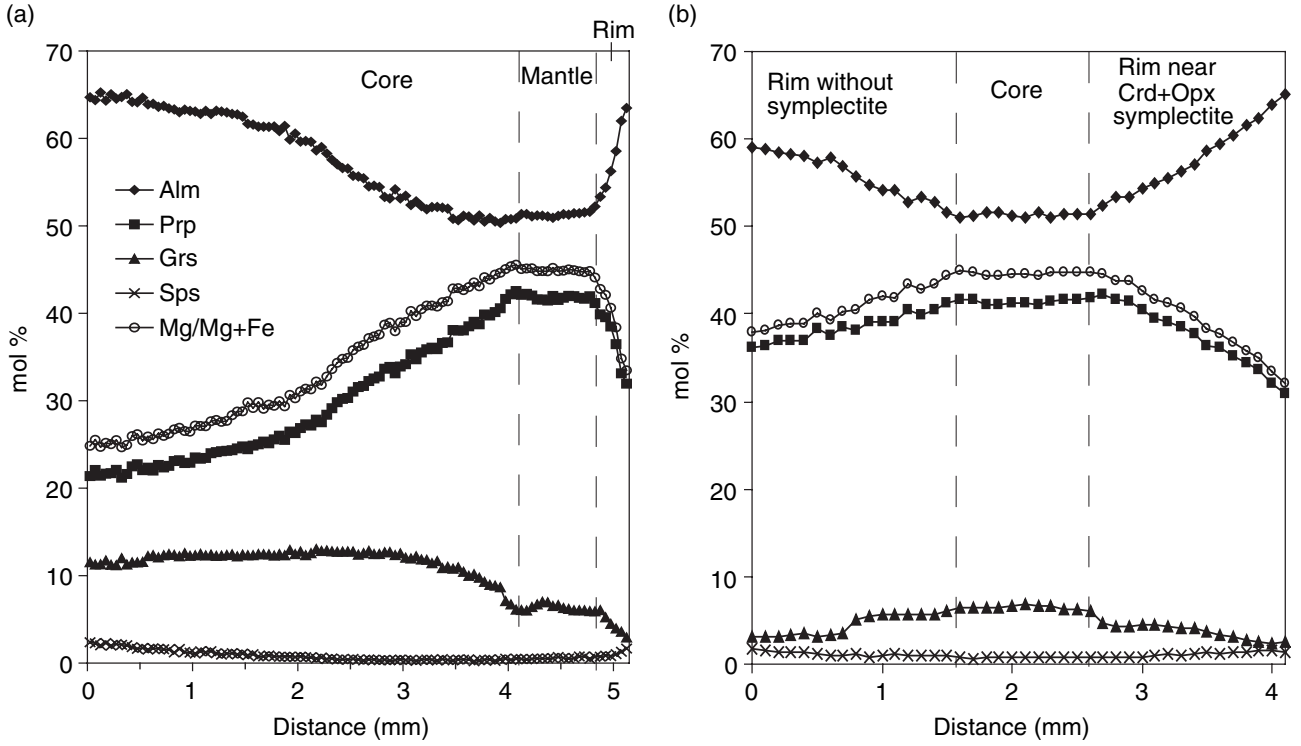


**Fig. 8.** Zoning profiles for garnet. (a) Zoning profile of almandine (Alm), pyrope (Prp), grossular (Grs) and spessartine (Sps) components and $X_{Mg}$ [=Mg/(Mg + Fe)] along the line A–B in Fig. 7(a). (b) Zoning profiles of a medium-grained matrix garnet. Note that the right part of the garnet rim is replaced by Crd + Opx symplectite, while the left rim is in contact with a matrix orthopyroxene.

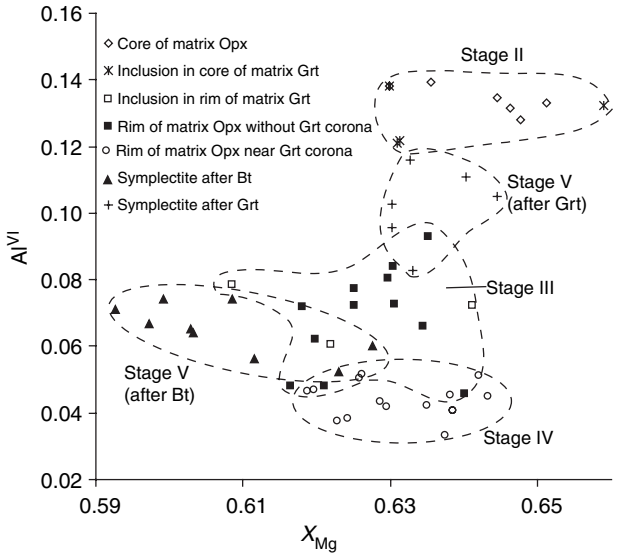


**Fig. 9.** Chemical composition of orthopyroxene plotted in terms of $Al^{VI}$ *v.* $X_{Mg}$ [=Mg/(Mg + Fe)].

almandine. The Fe–Mg zoning pattern of garnet is considered a result of retrograde Fe–Mg exchange among garnet, Opx and biotite. Compared with the core compositions, the rim of matrix orthopyroxene has much lower Al content; the rim of matrix biotite contains higher $Al^{VI}$. The rim of matrix plagioclase (Pl3) in contact with garnet become rich in anorthite, we infer that the increase of Ca in plagioclase rim (Pl3) and the decrease of Ca in nearby garnet are related to a net transfer reaction involving plagioclase, garnet, quartz and another aluminous phase (Spear, 1993). The aluminous phase is possibly kyanite, which is observed as inclusions in plagioclase (Fig. 2d). The modification of mineral compositions mentioned above is consistent with a cooling and decompression history after HP granulite facies metamorphism. The cooling history is also indicated by the precipitation of the ilmenite exsolution in the core of medium-grained orthopyroxene. An assemblage of Grt3 + Opx3 + Pl3 + Bt3 + Qtz is inferred for stage III.

The *P–T* conditions of stage III were calculated using compositions of Grt3, Opx3 and Pl3. In order to minimize the effect of late overprinting, only rim compositions of matrix minerals which are not overprinted by late garnet coronae, symplectites and kelyphites were used. Calculations on GO, GOPQ-1 and GOPQ-2 end-member reactions among garnet, orthopyroxene, plagioclase and quartz (see previous section) using THERMOCALC yield results of 630–700 °C and 4.8–6.0 kbar (Fig. 11). The *P–T* conditions of stage III were also calculated using the Grt–Opx thermometers of Harley (1984) and Bhattacharya *et al.*

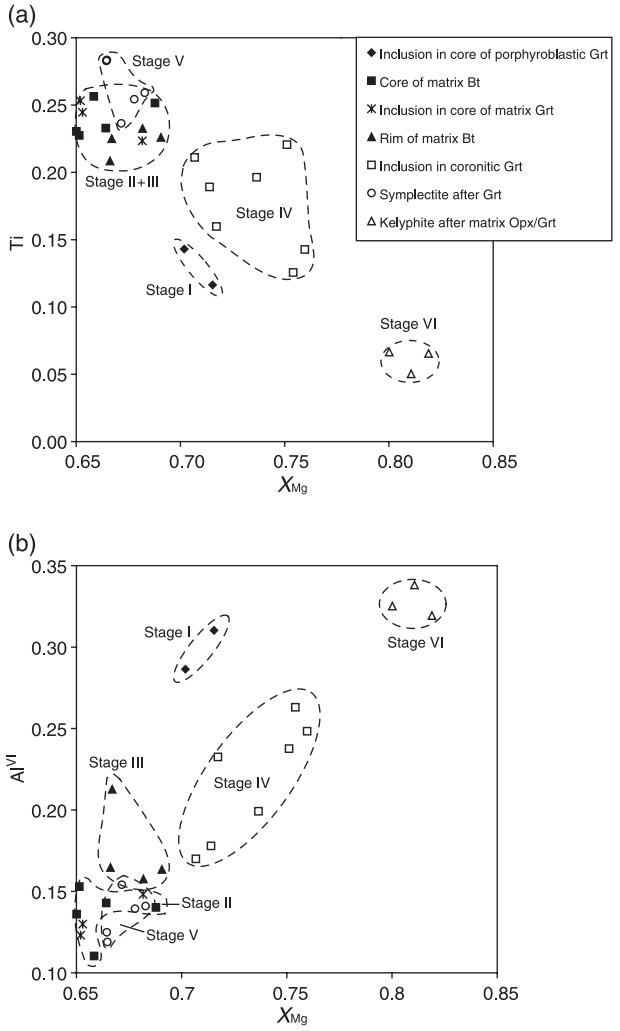


**Fig. 10.** Chemical composition of biotite, in terms of (a) Ti *v.* $X_{Mg}$ [=Mg/(Mg + Fe)] and (b) $Al^{VI}$ *v.* $X_{Mg}$.

(1991), the Grt–Opx–Pl–Qtz barometer of Newton & Perkins (1982) and Bhattacharya *et al.* (1991), and the Grt–Bt–Pl–Qtz barometer of Wu *et al.* (2004). The estimates fall in a narrow range of 660–740 °C and 5.4–6.9 kbar, which are slightly higher than the THERMOCALC results.

### Stage IV: medium pressure granulite facies metamorphism

The fourth stage of metamorphism is characterized by the occurrence of: (1) coronitic garnet (Grt4), with abundant quartz and rare plagioclase (Pl4) inclusions, between medium-grained matrix plagioclase and orthopyroxene (Fig. 3a,b); (2) coronitic garnet (Grt4), with abundant quartz and rare plagioclase (Pl4) and biotite (Bt4) inclusions, between medium-grained matrix plagioclase and biotite (Fig. 3c,d); and (3) coronitic garnet (Grt4) surrounding matrix pyrite. The garnet coronae outside orthopyroxene and biotite have similar compositions; however, garnet outside pyrite has slightly higher almandine component. The rim of coronitic garnet near plagioclase contains a higher grossular component than that near the mafic phases (Table 1, Fig. 6). The plagioclase inclusions (Pl4) in the coronitic garnet (Grt4) are richer in albite than the rim of matrix plagioclase (Pl3) away from the coronitic garnet. These features indicate that the formation of coronitic garnet preferentially consumed the anorthite component in plagioclase. The orthopyroxene rim (Opx4) near Grt4 is lower in $Al^{VI}$ than the rim of matrix orthopyroxene (Opx3) away from Grt4 (Fig. 9). The biotite inclusions (Bt4) in Grt4 have higher Mg and $Al^{VI}$ and lower Ti than the matrix biotite (Fig. 10). The mineral assemblage of stage IV is inferred to be Grt4 + Bt4 + Opx4 + Pl4 + Qtz.

Based on above textures and compositions, the following continuous reactions account for the formation of garnet corona:

$$\begin{aligned}&\mathrm{Opx3}(\mathrm{Al^{VI}} = 0.05 - 0.09) + \mathrm{Pl3}(\mathrm{An_{23-28}})\\ &\quad = \mathrm{Grt4} + \mathrm{Opx4}(\mathrm{Al^{VI}} = 0.03 - 0.05)\\ &\qquad + \mathrm{Pl4}(\mathrm{An_{19-21}}) + \mathrm{Qtz};\end{aligned} \quad (1)$$

and,

$$\begin{aligned}&\mathrm{Bt3}(X_{\mathrm{Mg}\,0.66-0.69}) + \mathrm{Pl3}(\mathrm{An_{23-28}}) = \mathrm{Grt4}\\ &\quad + \mathrm{Bt4}(X_{\mathrm{Mg}\,0.71-0.76}) + \mathrm{Pl4}(\mathrm{An_{19-21}}) + \mathrm{Qtz}.\end{aligned} \quad (2)$$

The textural and compositional features described in previous sections indicate that garnet formation occurred under relatively dry conditions and is diffusion-controlled. Equilibrium is assumed to reach only in limited reaction domains.

The *P–T* estimates for stage IV were attempted using compositions of coronitic garnet and minerals included in orthopyroxene–plagioclase reaction domain, which are not overprinted by later symplectite and kelyphite. The rim compositions of orthopyroxene (Opx4) and plagioclase (Pl4) in contact with coronitic garnet (Grt4) are also used. Calculations on GO, GOPQ-1 and GOPQ-2 end-member reactions among Grt4, Opx4, Pl4 and quartz using THERMOCALC yield 690–790 °C and 7.7–9.0 kbar (Fig. 11). *P–T* conditions of stage IV were also calculated using the Grt–Opx thermometers of Harley (1984) and Bhattacharya *et al.* (1991) and the Grt–Opx–Pl–Qtz barometers of Newton & Perkins (1982) and Bhattacharya *et al.* (1991). The estimates fall in a range of 740–790 °C and 8.2–9.3 kbar, which are slightly higher than the THERMOCALC results.

### Stage V: low-pressure/high-temperature granulite facies metamorphism

The fifth stage of metamorphism is recorded by: (1) replacement of porphyroblastic garnet (Grt3), matrix garnet (Grt3) and coronitic garnet (Grt4) by very fine-

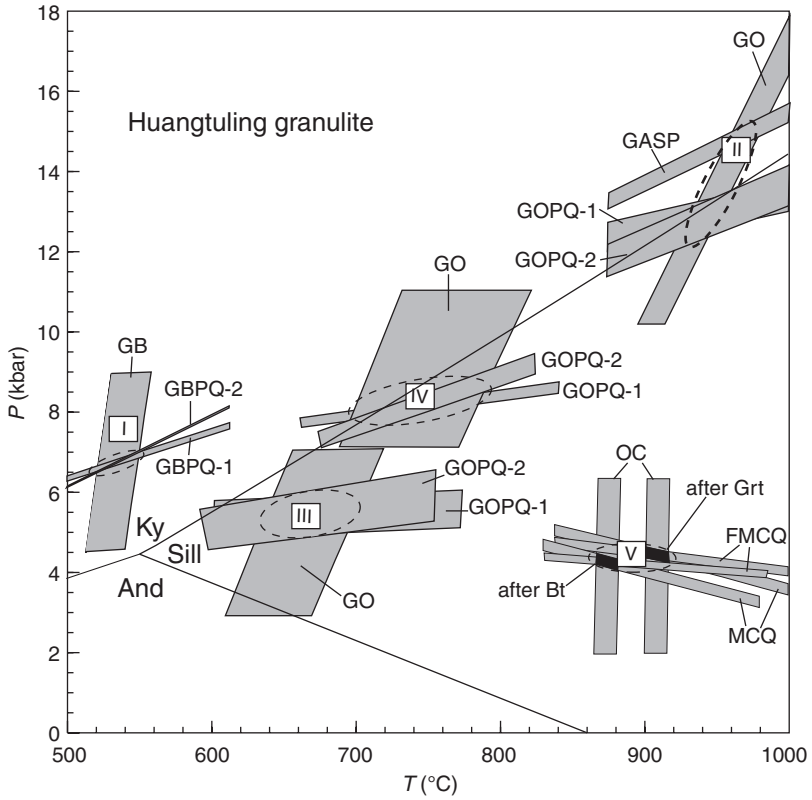


**Fig. 11.** *P–T* diagram showing results of THERMOCALC calculations based on representative end-member reactions using data from samples HTL11a (for stages I, II, V and VI), HTL19 (for stages II, III, IV, V and VI) and HTL24 (for stages I, II, III and IV). Aluminosilicate stability fields are calculated using THERMOCALC (Powell *et al.*, 1998) with internally consistent data set of Holland & Powell (1998). GB: Pyr + Ann = Alm + Phl; GBPQ-1: Prp + 2Grs + 3East + 6Qtz = 3Phl + 6An; GBPQ-2: Alm + 2Grs + 3East + 6Qtz = 2Phl + Ann + 6An; GO: 2Prp + 3Fs = 2Alm + 3En; GOPQ-1: 2Prp + Grs + 3Qtz = 3En + 3An; GOPQ-2: 2Alm + Grs + 3Qtz = 3Fs + 3An; GASP: Grs + 2Ky + Qtz = 3An; MCQ: 2Mgts + 3Qtz = Crd; OC: En + Fcrd = Fs + Crd; FMCQ: Fs + 2Mgts + 3Qtz = En + Fcrd.

grained symplectite of orthopyroxene (Opx5), cordierite (Crd5), biotite (Bt5), plagioclase (Pl5), spinel (Spl5), ilmenite and quartz (Fig. 4a–f); and (2) replacement of matrix biotite by symplectite of Opx5, Crd5 and quartz (Fig. 5a,b), which is consistent with dehydration melting of biotite at this stage. The grain size of symplectites after biotite is coarser than those after garnet. Crd5, Spl5 and quartz are commonly observed in direct contact in the symplectite after garnet, indicating ultrahigh or high-temperature metamorphism for stage V (Harley, 1998; Moraes & Fuck, 2000). This conclusion is consistent with high Cr in spinel, high Ti in biotite and high Ca ($An_{30-33}$) in plagioclase.

The symplectite after biotite can be accounted for by the following reactions:

$$\mathrm{Bt3 + Pl3 + Qtz = Opx5 + Crd5 + melt;} \quad (3)$$

and,

$$\mathrm{Bt3 + Pl3 = Crd5 \pm Opx5 + Qtz + melt.} \quad (4)$$

The following reactions can account for the formation of the symplectite after garnet:

$$\mathrm{Grt3/Grt4 + melt/fluid + Qtz = Opx5 + Crd5 + Bt5 + Pl5;} \quad (5)$$

and,

$$\mathrm{Grt3/Grt4 + melt/fluid = Crd5 + Bt5 + Qtz + Spl5 \pm Ilm.} \quad (6)$$

Minerals in different symplectitic domains, especially orthopyroxene, are of different compositions that are clearly controlled by their parent minerals. *P–T* conditions of stage V are calculated independently using compositions of symplectitic minerals after garnet and biotite.

The following three equilibria can describe reactions among components of cordierite, orthopyroxene and quartz in the symplectite:

$$\mathrm{2Mgts + 3Qtz = Crd(MCQ);}$$

$$\mathrm{En + Fcrd = Fs + Crd(OC);}$$

and,

$$\mathrm{Fs + 2Mgts + 3Qtz = En + Fcrd(FMCQ).}$$

Calculations on these reactions using THERMOCALC yield 4.3–4.7 kbar and 900–920 °C for symplectite after garnet, and 4.0–4.4 kbar and 860–880 °C for symplectite after biotite (Fig. 11).

Experiments on dehydration melting of biotite (Vielzeuf & Montel, 1994; Patiño Douce & Beard, 1995; Stevens *et al.*, 1997) indicate that the Opx-in reactions take place at temperatures higher than 850 °C at pressures of 4–5 kbar (Fig. 12), consistent with the calculated *P–T* estimates for stage V. Our calculated *P–T* conditions are also within the garnet breakdown field calculated in KFMASH system by White *et al.* (2001) (Fig. 13).

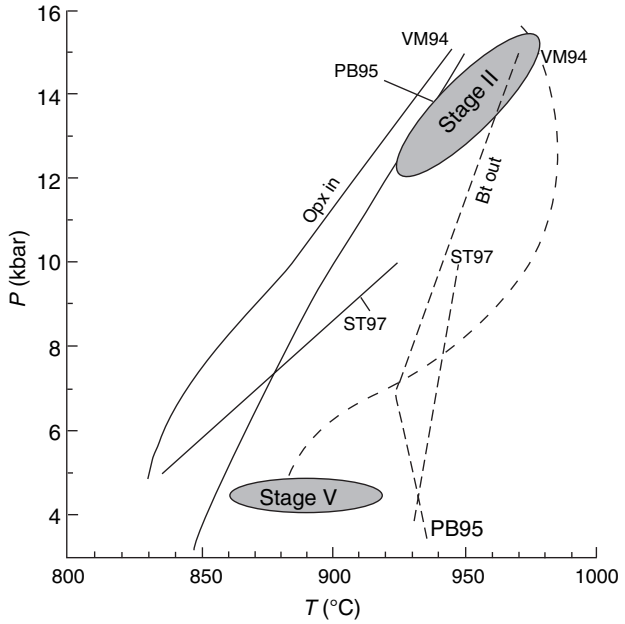


**Fig. 12.** *P–T* diagram showing the orthopyroxene-in (solid) and biotite-out (dashed) curves obtained from fluid-absent melting experiments. Shaded region is the estimated *P–T* conditions for stages II and V. VM94: Vielzeuf & Montel (1994); PB95: Patiño Douce & Beard (1995); ST97: Stevens *et al.* (1997).

### Stage VI: greenschist facies metamorphism

The last stage (stage VI) of metamorphism is recorded by the occurrence of chlorite (Chl6), low-Si muscovite (Ms6) and albite, which replace relict garnet, orthopyroxene and biotite in the matrix and symplectite assemblages. The compositions of Chl6, Bt6, Ms6 and Ab are used for *P–T* calculation of stage VI. End-member reactions among mineral assemblage of Chl6 + Bt6 + Ms + Pl + Qtz are calculated using THERMOCALC. These end-member reactions intersect in a narrow range of 1–2 kbar and 340–370 °C.

## DISCUSSION

### *P–T–t* history

The Huangtuling granulite had been dated by various methods. Three groups of ages have been reported. Ages of 2600–2800 Ma were obtained by SHRIMP (M. Sun, personal communication), SIMS (Wu *et al.*, 2002) and LA-ICPMS (Wu *et al.*, 2003) from rounded relict detrital zircon cores. These ages are interpreted as the age of the detrital zircon in the supercrustal sedimentary protolith of the Huangtuling granulite. Similar Pb–Pb SIMS ages of *c.* 2800 Ma were also

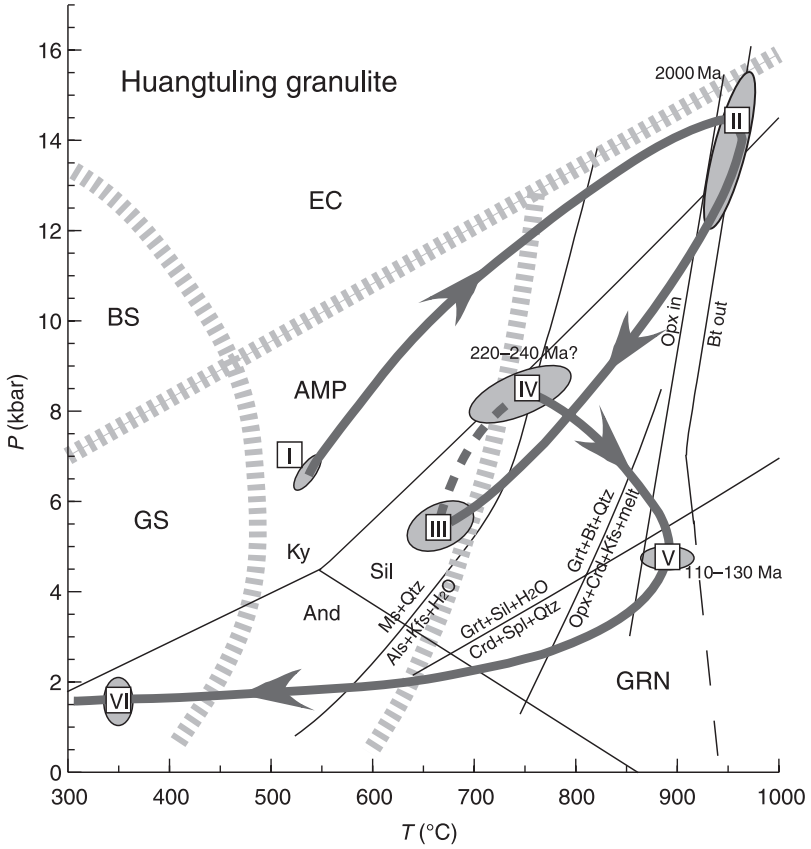


**Fig. 13.** *P–T–t* paths for the metamorphic evolution of Huangtuling granulite. Numbers refer to metamorphic stages in the text. Opx-in and Bt-out curves are after Patiño Douce & Beard (1995). Aluminosilicate stability fields are calculated using THERMOCALC (Powell *et al.*, 1998) with internally consistent data set of Holland & Powell (1998); boundaries of metamorphic facies are after Spear (1993). The breakdown reaction of muscovite (Ms + Qtz = Als + Kfs + $H_2O$) is after Spear *et al.* (1999). The univariant lines of Grt + Sil + $H_2O$ = Crd + Spl + Qtz and Grt + Bt + Qtz = Opx + Crd + Kfs + melt are after White *et al.* (2001). GS, greenschist facies; BS, blueschist facies; AMP, amphibolite facies; EC, eclogite facies; GRN, granulite facies.

obtained from relict detrital zircon cores from the surrounding migmatitic gneisses (Xia *et al.*, 2003).

Groups of *c.* 2000 Ma metamorphic ages were obtained by various methods from the Huangtuling granulite. Wu *et al.* (2002) reported 2052 ± 100 Ma SIMS U/Pb ages from low Th/U metamorphic overgrowth zircon rims, which is consistent with the more precise 1995–1982 Ma SHRIMP Pb–Pb zircon ages obtained by M. Sun (personal communication). Ages of *c.* 2000 Ma were also obtained by SIMS from metamorphic rims of zircon in the surrounding migmatitic gneisses (Xia *et al.*, 2003). Because the high-pressure/high-temperature granulite facies minerals (stage II) are predominant and the late-stage overprint is weak in Huangtuling granulite, we interpret the ages of *c.* 2000 Ma from low Th/U metamorphic zircon rims as the time of this metamorphic stage.

Cretaceous ages of 127 ± 9 Ma were obtained by the biotite-whole-rock Rb–Sr method from the Huangtuling granulite (Jian, 2001). It is inferred that the low-pressure/high-temperature granulite facies metamorphism (stage V) took place in the Cretaceous. The typical features of stage V are very high temperature ($>850$ °C) and breakdown of biotite. It is also inferred that the Rb–Sr system of biotite and whole rock might have been reset in stage V, and the *c.* 127 Ma Rb–Sr age denotes the cooling age of the high-temperature granulite. Cretaceous SIMS Th/U ages (*c.* 110 Ma) were also obtained from overgrowth zircon rims related to migmatization in the country gneisses of the Huangtuling granulite (Xia *et al.*, 2003), which are consistent with ages of granitoids and mafic–ultramafic plutons intruding the North Dabie metamorphic core complex (Hacker *et al.*, 1998; Jahn *et al.*, 1999; Ma *et al.*, 1999; Zhao *et al.*, 2005). The low-pressure/high-temperature granulite facies metamorphic event is contemporaneous with the pervasive migmatization of the regional gneisses (Xia *et al.*, 2003).

No zircon growth events can be attributed to the stage IV medium-pressure granulite facies metamorphism, which are inferred to be due to the lack of deformation during stage IV metamorphism, preventing infiltration of fluid. Textures and compositional features indicate that mineral reactions in stage IV were anhydrous and diffusion-controlled, so that most of the earlier stage minerals are preserved and metastable during this stage of metamorphism. Stage IV is interpreted to represent a crustal thickening event (Fig. 13). UHP eclogites occur in the north-eastern part of the North Dabie metamorphic core complex (Wei *et al.*, 1998; Xu *et al.*, 2003, 2005), indicating that the North Dabie complex was also involved in the Triassic subduction of Yangtze Craton underneath Sino-Korean Craton. Triassic ages were also reported from the migmatitic gneisses in the North Dabie metamorphic core complex (Liu *et al.*, 2000; Xie *et al.*, 2001, 2004; Jiang *et al.*, 2002; Liu & Li, 2005). Therefore, we attribute stage IV MP granulite facies metamorphism to the Triassic subduction-collision event.

### Tectonic implication of the HP granulite facies metamorphism

Stages I–III define a clockwise *P–T* path. The increase in *P–T* from stage I to stage II indicates that the supercrustal protolith of the Huangtuling granulite was buried to 40–50 km depth, implying a crustal thickening event at *c.* 2000 Ma. Stage III metamorphism indicates that the high-pressure granulites were exhumed to mid-crustal depth of 15–20 km. Similar Archean to Palaeoproterozoic HP granulites are reported in the Snowbird belt of Canada (Snoeyenbos *et al.*, 1995), Lewisian Complex of South Harris in NW Scotland (Baba, 1998), and Ubende belt in West Tanzania (Boven *et al.*, 1999). A Palaeo-Mesoproterozoic supercontinent, named Columbia, has been recently proposed (Rogers & Santosh, 2002; Zhao *et al.*, 2002, 2004). This supercontinent was assembled along global-scale collisional orogens at 2100–1800 Ma. To date, 2000 Ma high-grade metamorphic rocks are limited to the north margin of the Yangtze Craton (Zheng *et al.*, 2005), consistent with the location of the Huangtuling granulite. We propose that the northern margin of Yangtze Craton collided with an unknown cratonic block during the assembly of Columbia, and that the exhumation process of the HP granulite was probably related to late orogenic processes or breakup of the Columbia supercontinent.

### Metastability of the granulite during Triassic subduction

The prograde *P–T* path from stage III to stage IV represents another crustal thickening event, which we propose is related to the Triassic subduction/collision between the Yangtze and Sino-Korean Cratons. Preservation of stage II assemblages indicates that the HP granulite was metastable during Triassic orogenesis. Metastable textures also occur in other lower crustal rocks subducted to mantle depths, such as the mafic granulites from the Western Gneiss Region of Norway (e.g. Austrheim & Engvik, 1997; Wain *et al.*, 2001) and Haiyangsuo mafic granulites in the Sulu region (Ye *et al.*, 1999). Such metastable textures also are reported in gabbro, anorthosite and dolerite in the UHP metamorphic belts in the Sulu region of eastern China (Zhang & Liou, 1997), Caledonian Western Gneiss Region of Norway (Mørk, 1985) and the western Alps (Wayte *et al.*, 1989). Complete eclogitization only occurs along fractures or shear zones that acted as fluid conduits, whereas the dry host rocks away from fractures or shear zones retain metastable assemblage under HP and even UHP metamorphic conditions (Austrheim & Griffin, 1985; Mørk, 1985; Zhang & Liou, 1997; Bruno *et al.*, 2001; Wain *et al.*, 2001). These observations indicate that the metamorphic behaviour of the continental materials during subduction strongly depend on the presence or absence of deformation and a fluid phase (e.g. Rubie, 1986;

Austrheim, 1998). The absence of deformation and a fluid phase in stage IV results in the unique preservation of early-stage textures and minerals.

### Implications for the collapse of Dabie Orogen

The stage V low-pressure/high-temperature granulite facies metamorphism suggests that the rocks exhumated from at least 25 km to less than 15 km in the Cretaceous. The granulite was heated during uplift, accompanied by partial melting. Based on the following considerations, it is proposed that the entire North Dabie metamorphic core complex underwent heating, melting and exhumation: (1) the Cretaceous migmatization and granitoid magmatic intrusions are widespread (Ma *et al*., 2000); and (2) granulites from several other localities in the North Dabie metamorphic core complex also record high-temperature metamorphism at various depth (Zhang *et al*., 1996, 2000; Xiao *et al*., 2001, 2005).

The heat source for such high temperatures in the mid-crustal levels can only be achieved through either advective heat from asthenosphere upwelling or through removal or thinning of the mantle lithosphere (Carson *et al*., 1997; Gerbi *et al*., 2006). The time of collapse of the Dabie Orogen is contemporaneous with Cretaceous rifting and lithospheric thinning events in eastern China (e.g. Fan *et al*., 2000). The rift axis crosses the Dabie Orogen (Wu *et al*., 2005). The upwelling of asthenosphere accompanied by lithospheric rifting and thinning in eastern China provided heat for the high-temperature granulite facies metamorphism. This is evidenced by the simultaneous voluminous mantle-derived mafic to ultramafic plutons widespread in the North Dabie metamorphic core complex (Jahn *et al*., 1999; Wang *et al*., 2005; Zhao *et al*., 2005). The direct effect of mantle source material on the granulite is also evidenced by the occurrence of the unique Cr-rich spinel in the symplectite after garnet. Cr-rich spinel is only reported from ultramafic rocks with mantle origin (Dick & Bullen, 1984; Scowen *et al*., 1991; Barnes & Roeder, 2001), indicating that the granulite has been probably metasomatized by fluids or melts derived from a crystallizing mafic or ultramafic magma with mantle origin.

The voluminous upwelling of mantle-derived magmas must result in pervasive high-temperature granulite facies metamorphism and partial melting of the thickened crustal mountain root under the orogen. Partial melting of the thickened crustal root will significantly decrease the density and hence create an inverted density profile, with the migmatite in the basement of the orogen becoming less dense than the overlying cool crustal materials (Martinez *et al*., 2001). This could result in the buoyant exhumation of the migmatite terrane which encloses the granulite, such as those outcropped in north Dabie metamorphic core complex and the extensional thinning and collapse of the Dabie Orogen.

## CONCLUSIONS

**1.** The Huangtuling granulites in the North Dabie metamorphic core complex represent the lower continental crust of the subducted Yangtze Craton. These granulites preserve six stages of metamorphism: (I) an amphibolite facies metamorphism at 6.3–7.0 kbar and 520–550 °C; (II) a predominant high-pressure/high-temperature granulite facies metamorphism at 12–15.5 kbar and 920–980 °C; (III) a cooling and decompression history at 4.8–6.0 kbar and 630–700 °C; (IV) a medium-pressure granulite facies metamorphism at 7.7–9.0 kbar and 690–790 °C; (V) low-pressure/high-temperature granulite facies metamorphism at 4.0–4.7 kbar and 860–920 °C; (VI) greenschist facies metamorphic overprint at 1–2 kbar and 340–370 °C.

**2.** The Huangtuling granulite records two cycles of orogenic crustal thickening–thinning events. The earlier crustal thickening and thinning event occurred at *c*. 2000 Ma, possibly related to the assembly and breakup of the Columbia supercontinent. The later crustal thickening–thinning event is related to the Triassic subduction-collision between the Yangtze and Sino-Korean Cratons and Cretaceous collapse of the Dabie Orogen.

**3.** The dry lower crustal granulite was metastable during the Triassic subduction/collision because of the lack of deformation and fluid, which is in contrast with HP–UHP metamorphism in the subducted upper continental crust.

**4.** Asthenospheric upwelling or removal of the lithospheric mantle is required for reheating of the granulites and voluminous partial melting of the North Dabie metamorphic core complex that resulted in the extensional thinning and collapse of the Dabie Orogen.

## ACKNOWLEDGEMENTS

This work is supported by National Science Foundation of China (No. 40472046, 40421202 and 40523003) and the Chinese Academy of Sciences (KZCX3-SW-135, Bairenjihua 2005-192). Prof. Nengsong Chen in China University of Geosciences (Wuhan) is thanked for his help in the field work. Drs Q. Mao and Y. Ma are thanked for help in electron microprobe analysis. C. J. Wei and D. Moecher are thanked for their constructive reviews.

## REFERENCES

Andersen, T. B., 1998. Extensional tectonics in the Caledonides of southern Norway: an overview. *Tectonophysics*, **140,** 333–351.

Austrheim, H., 1998. The influence of fluid and deformation on metamorphism of the deep crust and consequences for the geodynamics of collision zones. In: *When Continents Collide: Geodynamics and Geochemistry of Ultra-High Pressure Rocks* (eds Hacker, B. & Liou, J.G.), pp. 297–323. Kluwer Academic Publishers, Dordrecht.

Austrheim, H. & Engvik, A., 1997. Fluid transport, deformation and metamorphism at depth in a collision zone. In: *Fluid Flow and Transport in Rocks: Mechanisms and Effects* (eds Jamtveit, B. & Yardley, B.), pp. 123–137. Chapman and Hall, London.

Austrheim, H. & Griffin, W. L., 1985. Shear deformation and eclogite formation within the granulite-facies anorthosites of the Beigen Arcs, Western Norway. *Chemical Geology*, **50,** 267–281.

Ayers, J. C., Dunkle, S. & Gao, S., 2002. Constraints on timing of peak and retrograde metamorphism in the Dabie Shan Ultrahigh-Pressure Metamorphic Belt, east-central China, using U–Th–Pb dating of zircon and monazite. *Chemical Geology*, **186,** 315–331.

Baba, S., 1998. Proterozoic anticlockwise P–T path of the Lewisian Complex of South Harris, Outer Hebrides, NW Scotland. *Journal of Metamorphic Geology*, **16,** 819–841.

Baird, D. J., Nelson, K. D., Knapp, J. H., Walters, J. J. & Brown, L. D., 1996. Crustal structure and evolution of the Trans-Hudson orogen: results from seismic reflection profiling. *Tectonics*, **15,** 416–426.

Baker, J., Matthews, A., Mattey, D., Rowley, D. & Xue, F., 1997. Fluid–rock interactions during ultra-high pressure metamorphism, Dabie Shan, China. *Geochimica et Cosmochimica Acta*, **61,** 1685–1696.

Barnes, S. J. & Roeder, P. L., 2001. The range of spinel compositions in terrestrial mafic and ultramafic rocks. *Journal of Petrology*, **42,** 2279–2302.

Berzin, R., Oncken, O., Knapp, J. H. *et al*., 1996. Orogenic evolution of the Ural Mountains: results from an integrated seismic experiment. *Science*, **274,** 220–221.

Bhattacharya, A., Krishnakumar, K. R., Raith, M. & Sen, S. K., 1991. An improve set of a–X parameters for Fe–Mg–Ca garnet and refinements of the orthopyroxene–garnet thermometer and the orthopyroxene–garnet–plagioclase-quartz barometer. *Journal of Petrology*, **32,** 629–656.

Boven, A., Theunissen, K., Sklyarov, E. *et al*., 1999. Timing of exhumation of a high-pressure mafic terrane of Paleoproterozoic Ubende belt (West Tanzania). *Precambrian Research*, **93,** 119–137.

Brown, M. & Dallmeyer, D., 1996. Rapid Variscan exhumation and the role of magma in core complex formation: southern Birttany metamorphic belt, France. *Journal of Metamorphic Geology*, **14,** 361–379.

Bruno, M., Compagnoni, R. & Rubbo, M., 2001. The ultra-high pressure coronitic and pseudomorphous reactions in a metagranodiorite from the Brossasco-Isasca Unit, Dora-Maira Massif, western Italian Alps: a petrographic study and equilibrium thermodynamic modeling. *Journal of Metamorphic Geology*, **19,** 33–43.

Carson, C. J., Powell, R., Wilson, C. J. L. & Dirks, P. H. G. M., 1997. Partial melting during tectonic exhumation of a granulite terrane: an example from the Larsemann Hills, East Antarctica. *Journal of Metamorphic Geology*, **15,** 105–126.

Carswell, D. A. & Compagnoni, R., 2003. Introduction with review of the definition, distribution and geotectonic significance of ultrahigh pressure metamorphism. In: *Ultrahigh Pressure Metamorphism* (eds Carswell, D. A. & Compagnoni, R.), pp. 3–9. Eotvos University Press, Budapest.

Chen, N. S., Sun, M., You, Z. D. & Malpas, J., 1998. Well-preserved garnet growth zoning in granulite from the Dabie Mountains, central China. *Journal of Metamorphic Geology*, **16,** 213–222.

Dale, J., Powell, R., White, R. W., Elmer, F. L. & Holland, T. J. B., 2005. A thermodynamic model for Ca–Na clinoamphiboles in $Na_2O$–CaO–FeO–MgO–$Al_2O_3$–$SiO_2$–$H_2O$–O for petrological calculations. *Journal of Metamorphic Geology*, **23,** 771–791.

Dick, H. J. B. & Bullen, T., 1984. Chromian spinel as a petrogenetic indicator in abyssal and alphine-type peridotites and spatially associated lavas. *Contributions to Mineralogy and Petrology*, **86,** 54–76.

Echtler, H. P., Stiller, M., Steinhoff, F., *et al*. 1996. Preserved collisional crustal structure of the Southern Urals revealed by vibroseis profiling. *Science*, **274,** 224–226.

Ernst, W. G., 2001. Subduction, ultrahigh-pressure metamorphism, and regurgitation of buoyant crustal slices – implications for arcs and continental growth. *Physics of The Earth and Planetary Interiors*, **127,** 253–275.

Fan, W. M., Zhang, H. F., Baker, J., Jarvis, K. E., Mason, P. R. D. & Menzies, M. A., 2000. On and off the North China Craton: where is the Archaean keel? *Journal of Petrology*, **41,** 933–950.

Fu, B., Touret, J. L. R., Zheng, Y. F. & Jahn, B. M., 2003. Fluid inclusions in granulites, granulitized eclogites and garnet clinopyroxenite from the Dabie–Sulu terranes, eastern China. *Lithos*, **70,** 293–319.

Gao, S., Zhang, B. R., Jin, Z. M., Kern, H., Luo, T. C. & Zhao, Z. D., 1998. How mafic is the lower continental crust? *Earth and Planetary Science Letters*, **161,** 101–117.

Gerbi, C. C., Johnson, S. E. & Koons, P. O., 2006. Controls on low-pressure anatexis. *Journal of Metamorphic Geology*, **24,** 107–118.

Hacker, B. R., Ratschbacher, L., Webb, L., Ireland, T., Walker, D. & Dong, S. W., 1998. U/Pb zircon ages constrain the architecture of the ultrahigh-pressure Qinling-Dabie orogen, China. *Earth and Planetary Science Letters*, **161,** 215–230.

Hacker, B. R., Ratschbacher, L., Webb, L. *et al*., 2000. Exhumation of ultrahigh-pressure continental crust in East-central China: Late Triassic–Early Jurassic tectonic unroofing. *Journal of Geophysical Research*, **105,** 13339–13364.

Harley, S. L., 1984. An experimental study of the partitioning of Fe and Mg between garnet and orthopyroxene. *Contributions to Mineralogy and Petrology*, **86,** 359–373.

Harley, S. L., 1998. On the occurrence and characterization of ultrahigh-temperature crustal metamorphism. In: *What Drives Metamorphism and Metamorphic Reactions* (eds Treloar, P. J. & O'Brien, P. J.), *Geological Society of London Special Publications*, **138,** 81–107.

Holdaway, M. J., 2000. Application of new experimental and garnet Margules data to the garnet–biotite thermometer. *American Mineralogists*, **85,** 881–892.

Holdaway, M. J., 2001. Recalibration of the GASP geobarometer in light of recent garnet and plagioclase activity models and versions of the garnet-biotite geothermometer. *American Mineralogists*, **86,** 1117–1129.

Holland, T. J. B. & Powell, R., 1998. An internally consistent thermodynamic data set for phase of petrological interest. *Journal of Metamorphic Geology*, **16,** 309–343.

Jahn, B. M., Wu, F. Y., Lo, C. H. & Tsai, C. H., 1999. Crust-mantle interaction induced by deep subduction of the continental crust: geochemical and Sr–Nd isotopic evidence from post-collisional mafic-ultramafic intrusions of the northern Dabie complex, central China. *Chemical Geology*, **157,** 119–146.

Jian, P., 2001. Rb–Sr mica dating of high-grade metamorphic rocks from the Dabie Mountains and its geological significance. *Acta Geoscientia Sinica*, **22,** 409–412 (Chinese with English abstract).

Jiang, L. L., Liu, Y. C. & Wu, W. P., 2002. Zircon U–Pb age and its geological implications of the gray gneiss to the northern Manshuihe in the North Dabie Mountains. *Geochimica*, **31,** 66–70 (in Chinese with English abstract).

Knapp, J. H., Diaconescu, C. C., Bader, M. A., Sokolov, V. B., Kashubin, S. N. & Rybalka, A. V., 1998. Seismic reflection fabrics of continental collision and post-orogenic extension in the Middle Urals, central Russia. *Tectonophysics*, **288,** 115–126.

Kretz, R., 1983. Symbols for rock-forming minerals. *American Mineralogists*, **68,** 277–279.

Le Pichon, X., Henry, P. & Goffé, B., 1997. Uplift of Tibet: from eclogites to granulites – implications for the Andean Plateau and the Variscan belt. *Tectonophysics*, **273,** 57–76.

Leake, B. E., Wooley, A. R., Arps, C. E. S. *et al.* 1997. Nomenclature of amphiboles: report of the subcommittee on amphiboles of the international mineralogical association, commission on new minerals and mineral names. *Canadian Mineralogist*, **35,** 219–246.

Li, S. G., Xiao, Y., Liu, D., Chen, Y., *et al.* 1993. Collision of the North China and Yangtze blocks and formation of coesite-bearing eclogites: timing and processes. *Chemical Geology*, **109,** 89–111.

Li, S. G., Jagoutz, E., Chen, Y. Z. & Li, Q. L., 2000. Sm–Nd and Rb–Sr isotopic chronology and cooling history of ultrahigh pressure metamorphic rocks and their country rocks at Shuanghe in the Dabie Mountains, Central China. *Geochimica et Cosmochimica Acta*, **64,** 1077–1093.

Liou, J. G., 1999. Petrotectonic summary of less intensively studied UHP regions. *International Geology Review*, **41,** 571–586.

Liu, Y. C. & Li, S. G., 2005. Lower crustal rocks from the Dabie Mountains and their deep subduction. *Acta Petrologica Sinica*, **21,** 1059–1066 (in Chinese with English abstract).

Liu, Y. C., Li, S. G. & Xu, S. T., 2000. U–Pb zircon ages of the eclogite and tonalitic gneiss from the northern Dabie Mountains, China and multi-overgrowths of metamorphic zircons. *Geological Journal of China Universities*, **6,** 417–423 (in Chinese with English abstract).

Mørk, M. B. E., 1985. A gabbro to eclogite transition on Flemsøy, Sunnmøre, western Norway. *Chemical Geology*, **50,** 283–310.

Ma, C. Q., Yang, K. G., Xu, C. H., Li, Z. C. & Ehlers, C., 1999. Mesozoic potassic magmatism in the Dabie Mountains: implication for exhumation mechanism of ultrahigh-pressure metamorphic terranes. *Acta Petrologica Sinica*, **15,** 379–395 (in Chinese with English abstract).

Ma, C. Q., Ehlers, C., Xu, C. H., Li, Z. C. & Yang, K. G., 2000. The roots of the Dabieshan ultrahigh-pressure meyamorphic terrane: constraints from geochemistry and Nd-Sr isotope systematics. *Precambrian Research*, **102,** 279–301.

Martinez, F., Goodliffe, A. M. & Taylor, B., 2001. Metamorphic core complex formation by density inversion and lower-crust extrusion. *Nature*, **411,** 930–934.

Milnes, A. G., Wennberg, O. P., Skår & Koestler, A. G., 1997. Contraction, extension and timing in the South Norwegian Caledonides: the Sognefjord transect. In: *Orogeny Through Time* (eds Burg, J.P. & Ford, M.), *Geological Society, Special Publications*, **140,** 123–148.

Moraes, R. D. & Fuck, R. A., 2000. Ultra-high-temperature metamorphism in Central Brazil: the Barro Alto complex. *Journal of Metamorphic Geology*, **18,** 345–358.

Myrow, P. M., Hughes, N. C., Paulsen, T. S., *et al.* 2003. Integrated tectonostratigraphic analysis of the Himalaya and implications for its tectonic reconstruction. *Earth and Planetary Science Letters*, **212,** 433–441.

Nelson, K. D., 1992. Are crustal thickness variations in old mountain belts like the Appalachians a consequence of lithospheric delamination? *Geology*, **20,** 498–502.

Nelson, K. D., Baird, D. J., Walters, J. J., *et al.* 1993. Trans-Hudson Orogen and Williston Basin in Montana and North Dakota: new COCORP deep-profiling results. *Geology*, **21,** 447–450.

Nelson, K. D., Zhao, W. J., Brown, L. D., *et al.* 1996. Partially molten middle crust beneath Southern Tibet: synthesis of project INDEPTH results. *Science*, **274,** 1684–1688.

Newton, R. C. & Perkins, D., 1982. Thermodynamic calibration of geobarometers based on the assemblages garnet–plagioclase–othopyroxene (clinopyroxene)–quartz. *American Mineralogists*, **67,** 203–222.

O'Brien, P. J., 2001. Subduction followed by collision: Alpine and Himalayan examples. *Physics of The Earth and Planetary Interiors*, **127,** 277–291.

Okay, A. I., Sengor, A. M. C. & Satir, M., 1993. Tectonics of an ultrahigh-pressure metamorphic terrane: Dabie Shan, China. *Tectonics*, **12,** 1320–1334.

Patiño Douce, A. E. & Beard, J. S., 1995. Dehydration-melting of biotite gneiss and quartz amphibolite from 3 to 15 kbar. *Journal of Petrology*, **36,** 707–738.

Pfiffner, O. A., Ellis, S. & Beaumount, C., 2000. Collision tectonics in the Swiss Alps: insight from geodynamic modeling. *Tectonics*, **19,** 1065–1094.

Powell, R., Holland, T. J. B. & Worley, B., 1998. Calculating phase diagrams involving solid solutions via nonlinear equations, with examples using Thermocalc. *Journal of Metamorphic Geology*, **16,** 577–588.

Ratschbacher, L., Hacker, B. R., Webb, L. E., et al., 2000. Exhumation of ultrahigh-pressure continental crust in east-central China: Cretaceous and Cenozoic unroofing and the Tan–Lu fault. *Journal of Geophysical Research*, **105,** 13303–13338.

Rogers, J. J. W. & Santosh, M., 2002. Configuration of Columbia, a Mesoproterozoic Supercontinent. *Gondwana Research*, **5,** 5–22.

Rolfo, F., Compagnoni, R., Wu, W. P. & Xu, S. T., 2004. A coherent lithostratigraphic unit in the coesite-eclogite complex of Dabie Shan, China: geologic and petrologic evidence. *Lithos*, **73,** 71–94.

Rowley, D. B., Xue, F., Tucker, R. D., Peng, Z. X., Baker, J. & Davis, A., 1997. Ages of ultrahigh pressure metamorphism and protolith orthogneisses from the eastern Dabie Shan: U/Pb zircon geochronology. *Earth and Planetary Science Letters*, **151,** 191–203.

Rubie, D. C., 1986. The catalysis of mineral reactions by water and restrictions on the presence of aqueous fluid during metamorphism. *Mineralogical Magazine*, **50,** 399–415.

Scowen, P. A. H., Roeder, P. L. & Helz, R. T., 1991. Reequilibration of chromite within Kilaues Iki lava, Hawaii. *Contributions to Mineralogy and Petrology*, **107,** 8–20.

Snoeyenbos, D. R., Williams, M. L. & Hanmer, S., 1995. Archean high-pressure metamorphism in the western Canadian Shield. *European Journal of Mineralogy*, **7,** 1251–1272.

Spear, F. S., 1993. *Metamorphic Phase Equilibria and Pressure–Temperature–Time Paths. Mineralogical Society of America Monograph*. Mineralogical Society of America, Washington, DC.

Spear, F. S., Kohn, M. J. & Cheney, J. T., 1999. P–T paths from anatectic pelites. *Contributions to Mineralogy and Petrology*, **134,** 17–32.

Stevens, G., Clemens, J. D. & Droop, G. T. R., 1997. Melt production during granulite-facies anatexis: experimental data from "primitive" metasedimentary protoliths. *Contributions to Mineralogy and Petrology*, **128,** 352–370.

Vielzeuf, D. & Montel, J. M., 1994. Partial melting of metagreywackes. Part I. Fluid-absent experiments and phase relationships. *Contributions to Mineralogy and Petrology*, **117,** 375–393.

Wain, A. L., Waters, D. J. & Austrheim, H., 2001. Metastability of granulites and process of eclogitisation in the UHP region of western Norway. *Journal of Metamorphic Geology*, **19,** 609–625.

Wang, C. Y., Zeng, R. S., Mooney, W. D. & Hacker, B. R., 2000. A crustal model of the ultrahigh-pressure Dabie Shan orogenic belt, China, derived from deep seismic refraction profiling. *Journal of Geophysical Research*, **105,** 10857–10869.

Wang, Y. J., Fan, W. M., Peng, T. P., Zhang, H. F. & Guo, F., 2005. Nature of the Mesozoic lithospheric mantle and tectonic decoupling beneath the Dabie Orogen, Central China: evidence from $^{40}Ar/^{39}Ar$ geochronology, elemental and Sr–Nd–Pb isotopic compositions of early Cretaceous mafic igneous rocks. *Chemical Geology*, **220,** 165–189.

Wayte, G. J., Worden, R. H., Rubie, D. C. & Droop, G. T. R., 1989. A TEM study of disequilibrium plagioclase breakdown at high pressure: the role of infiltrating fluid. *Contributions to Mineralogy and Petrology*, **101,** 426–437.

Wei, C. J., Shan, Z. G., Zhang, L. F., Wang, S. G. & Chang, Z. G., 1998. Determination and geological significance of the

eclogites from the northern Dabie Mountains, central China. *Chinese Science Bulletin*, **43,** 253–256.

White, A. P. & Hodges, K. V., 2003. Pressure–temperature–time evolution of the Central east Greenland Caledonides: quantitative constraints on crustal thickening and synorogenic extension. *Journal of Metamorphic Geology*, **21,** 875–897.

White, R. W., Powell, R. & Holland, T. J. B., 2001. Calculation of partial melting equilibria in the system $Na_2O$–CaO–$K_2O$–FeO–MgO–$Al_2O_3$–$SiO_2$–$H_2O$ (NCKFMASH). *Journal of Metamorphic Geology*, **19,** 139–153.

Wu, Y. B., Chen, D. G., Xia, Q. K., Deloule, E. & Chen, H., 2002. SMS U–Pb dating of zircons in granulite of Huangtuling from Northern Dabieshan. *Acta Petrologica Sinica*, **18,** 378–382 (in Chinese with English abstract).

Wu, Y. B., Chen, D. G., Xia, Q. K., Tu, X. L., Chen, H. & Yang, X. Z., 2003. In-situ trace element analyses and Pb–Pb dating of zircons in granulite from Huangtuling, Dabieshan by LAM-ICP-MS. *Science in China*, **46,** 1161–1170.

Wu, C. M., Zhang, J. & Ren, L. D., 2004. Empirical garnet–biotite–plagioclase–quartz geobarometry in medium- to high-grade metapelites. *Journal of Petrology*, **45,** 1907–1921.

Wu, F. Y., Lin, J. Q., Wilde, S. A., Zhang, X. O., Yang, J. H., 2005. Nature and significance of the Early Cretaceous giant igneous event in eastern China. *Earth and Planetary Science Letters*, **233,** 103–119.

Xia, Q. K., Zheng, Y. F., Ge, N. J. & Deloule, E., 2003. U–Pb ages and oxygen isotope compositions of zircons from gneiss of Huangtuling, Northern Dabie: old protolith and multi-stage evolution. *Acta Petrologica Sinica*, **19,** 506–512 (in Chinese with English abstract).

Xiao, Y. L., Hoefs, J., Van Den Kerkhof, A.M. & Li, S.G, 2001. Geochemical constraints of the eclogite and granulite facies metamorphism as recognized in the Raobazhai complex from North Dabie Shan, Chin. *Journal of Metamorphic Geology*, **19,** 3–19.

Xiao, Y. L., Hoefs, J. & Kronz, A., 2005. Compositionally zoned Cl-rich amphiboles from North Dabie Shan, China: monitor of high-pressure metamorphic fluid/rock interaction processes. *Lithos*, **81,** 279–295.

Xie, Z., Chen, J. F. & Zhang, X., 2001. Zircon U–Pb dating of gneiss from Shizhuhe in North Dabie and its geologic implications. *Acta Petrologica Sinica*, **17,** 139–144 (in Chinese with English abstract).

Xie, Z., Gao, T. S. & Chen, J., 2004. Multi-stage evolution of gneiss from North Dabie: evidence from zircon U–Pb chronology. *Chinese Science Bulletin*, **49,** 1963–1969.

Xu, S. T., Liu, Y., Chen, G. *et al*., 2003. New finding of microdiamands in eclogites from Dabie–Sulu region in central-eastern China. *Chinese Science Bulletin*, **48,** 988–994.

Xu, S. T., Liu, Y. C., Chen, G. B., Ji, S. Y., Ni, P. & Xiao, W. S., 2005. Microdiamonds, their classification and tectonic implications for the host eclogites from the Dabie and Sulu regions in central eastern China. *Mineralogical Magazine*, **69,** 509–520.

Xue, F., Rowley, D. B., Tucker, R. D. & Peng, Z. X., 1997. U–Pb zircon ages of granitoid rocks in the north Dabie complex, eastern Dabie Shan, China. *Journal of Geology*, **105,** 744–753.

Ye, K., Cong, B. L., Hirajima, T. & Banno, S., 1999. Transformation from granulite to transitional eclogite at Haiyangsuo, Rushan Country, eastern Shangdong Peninsula: the kinetic process and tectonic implications. *Acta Petrologica Sinica*, **15,** 21–36.

Yui, T. F., Rumble, D., Chen, C. H. & Lo, C. H., 1997. Stable isotope characteristics of eclogites from the ultra-high-pressure metamorphic terrain, central-east China. *Chemical Geology*, **137,** 135–147.

Zhang, R. Y. & Liou, J. G., 1997. Partial transformation of gabbro to coesite-bearing eclogite from Yangkou, the Sulu terrane, eastern China. *Journal of Metamorphic Geology*, **15,** 183–202.

Zhang, R. Y., Liou, J. G. & Tsai, C. H., 1996. Petrogenesis of a high-temperature metamorphic terrane: a new tectonic interpretation for the north Dabieshan, central China. *Journal of Metamorphic Geology*, **14,** 319–334.

Zhang, Z. M., Zhong, Z. Q., You, Z. D. & Hu, K. M., 2000. Granulite-facies retrograde metamorphism of garnet pyroxenite in Muzidian, northern Dabie Mountain. *Earth Science-Journal of China University of Geosciences*, **25,** 295–301 (in Chinese with English abstract).

Zhang, H. F., Gao, S., Zhong, Z. Q., Zhang, B. R., Zhang, L. & Hu, S. H., 2002. Geochemical and Sr–Nd–Pb isotopic compositions of Cretaceous granitoids: constraints on tectonic framework and crustal structure of the Dabieshan ultrahigh-pres sure metamorphic belt, Chin. *Chemical Geology*, **186,** 281–299.

Zhao, W. J. & Nelson, K. D., 1993. Project INDEPTH Team, Deep seismic reflection evidence for continental underthrusting beneath southern Tibet. *Nature*, **366,** 557–559.

Zhao, G. C., Cawood, P. A., Wilde, S. A. & Sun, M., 2002. Review of global 2.1–1.8 Ga orogens: implications for a pre-Rodinia supercontinent. *Earth-Science Reviews*, **59,** 125–162.

Zhao, G. C., Sun, M., Wilde, S. A. & Li, S., 2004. A Paleo-mesoproterozoic supercontinent: assembly, growth and breakup. *Earth-Science Reviews*, **67,** 91–123.

Zhao, Z. F., Zheng, Y. F., Wei, C. S., Wu, Y. B., Chen, F. K. & Jahn, B. M., 2005. Zircon U–Pb age, element and C–O isotope geochemistry of post-collisional mafic-ultramafic rocks from the Dabie orogen in east-central China. *Lithos*, **83,** 1–28.

Zheng, Y. F., Fu, B., Li, Y. L., Xiao, Y. L. & Li, S. G., 1998. Oxygen and hydrogen isotope geochemistry of ultrahigh pressure eclogites from the Dabie Mountains and the Sulu terrane. *Earth and Planetary Science Letters*, **155,** 113–129.

Zheng, Y. F., Zhou, J. B., Wu, Y. B. & Xie, Z., 2005. Low-grade metamorphic rocks in the Dabie-Suli orogenic belt: a passive-margin accretionary wedge deformed during continent subduction. *International Geology Review*, **47,** 851–871.

*Received 20 March 2006; revision accepted 27 June 2006.*